Industrial Crops & Products 218 (2024) 118907

Contents lists available at ScienceDirect

Industrial Crops & Products

journal homepage: www.elsevier.com/locate/indcrop

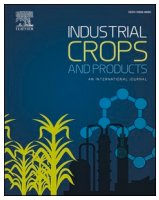

Hydro-processing of palm fatty acid distillate for diesel-like hydrocarbon fuel production using La-zeolite beta catalyst

I. Nur Azreena [a,*], N. Asikin-Mijan [d], H.L.N. Lau [a], M.A. Hassan [e], S. Mohd Izham [b,c], E. Kennedy [f], M. Stockenhuber [f], P. Yan [f,g], Y.H. Taufiq-Yap [b]

[a] Engineering and Processing Division, Biomass Technology Unit, Malaysian Palm Oil Board, No 6, Persiaran Institusi, Kajang, Selangor 43000, Malaysia
[b] Catalysis Science and Technology Research Centre, Faculty of Science, Universiti Putra Malaysia, Serdang, Selangor 43400 UPM, Malaysia
[c] Department of Chemistry, Faculty of Science, Universiti Putra Malaysia, Serdang, Selangor 43400 UPM, Malaysia
[d] Department of Chemical Sciences, Faculty of Science and Technology, Universiti Kebangsaan Malaysia, Bangi, Selangor Darul Ehsan 43600 UKM, Malaysia
[e] Department of Bioprocess Technology, Faculty of Biotechnology and Biomolecular Sciences, Universiti Putra Malaysia, Serdang, Selangor 43400, Malaysia
[f] Chemical Engineering, School of Engineering, University of Newcastle, Callaghan, NSW 2308, Australia
[g] School of Chemical Engineering, The University of Queensland, St Lucia, QLD 4072, Australia

ARTICLE INFO

Keywords:
Renewable diesel
Hydrodeoxygenation
PFAD
Zeolite beta
Lanthanum

ABSTRACT

Green diesel produced from palm fatty acid distillate (PFAD) could decrease reliance on fossil fuels and GHG emissions. Thus, this work reports a solventless hydrodeoxygenation (HDO) reaction using zeolite beta and La-zeolite beta (LZ) to convert PFAD into diesel-rich fuel. Specifically, LZ-catalyzed reaction dominated the hydrocarbon fraction over zeolite beta with high HDO and DO activity. Lewis' acid sites remove oxygenated species, while Brønsted acid sites aid in cracking. Since most HDO reactions happened on LZs' exteriors, pore size did not affect HDO. The HDO optimum reaction activity was attained at 400 °C using 1 wt% of LZ under 5 MPa H_2 pressure within 3 h. LZ showed 84 % diesel selectivity and greater hydrocarbon output in the N_2 flow environment (DO reaction) than the H_2-reaction conditions. The H_2 atmospheric reaction system prevented LZ coking, confirming its effect on catalyst stabilisation. The HDO process yielded a paraffinic hydrocarbon product with ~73 % selectivity of hexadecane (C16H34), demonstrating the formation of liquid fuel with reduced oxygenates. A vacuum distillation technique purified the crude liquid product (CLP) into a refined liquid product (RLP) with 99 % diesel component renewable diesel (RD 100) met ultra-low sulfur diesel requirements that closely resemble those derived from petroleum. This affirms that the high-quality R100 can be used in existing diesel engines efficiently without modifications. Based on reusability studies, the LZ catalysts are capable of performing HDO and DO for up to 5–6 cycles, proving their positive impact on process efficiency and catalyst longevity. Overall, the LZ-catalyzed hydrogen-assisted process is a more promising technology for the oil and gas industry, where hydrogen can be produced from various refinery feedstocks, hence, its implementation could significantly enhance efficiency and sustainability in refining operations.

1. Introduction

The depletion of fossil fuel reserves and the global warming associated with excessive CO_2 emissions have driven the demand for innovative and sustainable transportation energy sources (Wan Khalit et al., 2021). Biodiesel, a widely considered alternative biofuel, is hindered by inherent issues like poor cold flow characteristics and weak oxidation stability. These drawbacks pose challenges, rendering its practical application as a transportation fuel unfeasible (Aziz et al., 2024). Moroever, biodiesel typically contain higher oxygenates species, which results in problems that limit their utilization such as: lower heat of combustion, higher hygroscopicity and higher reactivity with other materials. Due to this reason, liquid hydrocarbons that are chemically fungible with fossil fuels are therefore required. Noted, the only fossil fuel substitute available is green diesel due to their similarities to fossil fuels (Abdulkareem-alsultan et al., 2021).

Malaysia, as the world's second-largest palm oil producer after Indonesia, produces more than 700,000 metric ton of palm fatty acid distillate (PFAD) annually (Lam et al., 2022). PFAD is a lower-value by-product which is generated in the fatty acid stripping and

* Corresponding author.
E-mail address: nurazreenaidris@gmail.com (I. Nur Azreena).

https://doi.org/10.1016/j.indcrop.2024.118907
Received 18 February 2024; Received in revised form 30 May 2024; Accepted 3 June 2024
Available online 21 June 2024

deodorization stages. It is potentially a valuable, low-cost feedstock for the production of green diesel. Indeed, PFAD mainly comprised of free fatty acid (FFA) ~80 %-rich of oxygenated species. As mentioned earlier, oxygenated species are problematic and should be eliminated. One of the most important research area in transformation of fatty acid is catalytic hydrodeoxygenation (HDO) and deoxygenation (DO) (Somnuk et al., 2020). By enabling the efficient conversion of PFAD into high-quality green diesel, this technology helps reduce reliance on fossil fuels. Biofuels derived from PFAD potentially have a lower carbon footprint compared to fossil fuels, assuming sustainable practices in palm oil production and processing. This contributes to the reduction of greenhouse gas (GHG) emissions, aligning with global climate change mitigation efforts (Xu et al., 2020).

The HDO of fatty acids is a process of removing oxygen to produces alkanes (C_n) with the same number as the corresponding fatty acid chain in the form of water (H_2O). Meanwhile, DO of fatty acids is a process that removes oxygen atoms in the form of H_2O or carbon oxides (CO_x) in order to produce green diesel or hydrocarbons that resemble diesel from renewable sources. Reaction pathways for the DO of fatty acids consist of decarboxylation (DCX) and decarbonylation (DCN). The DCX produces CO_2 and n-alkanes with the loss of one carbon atom (C_{n-1}) from the original fatty acid feedstock (C_n). In case of DCN, both CO and H_2O are lost from the original fatty acid feedstock while alkenes are generated (Thongkumkoon et al., 2019). Noted, both of these processes generated long-chain deoxygenated hydrocarbons with a high cetane number, making it fully compatible with fossil diesel fuel and provides a promising approach for the production of renewable diesel-like hydrocarbons (Han et al., 2011). Note, in term of economic viability, DO route is highly preferable than HDO which consume much hydrogen during the reaction. Nevertheless, HDO product that contained saturated species showed superior properties such as high calorific values, more stable and less reactive product, and more efficient and cleaner combustion, reducing emissions of pollutants during the burning of biofuels, and the biofuels derived from saturated HDO can be seamlessly integrated into the existing biodiesel production facilities (Mailaram and Maity, 2019).

Noteworthy, catalyst has a crucial role in determining the yield of liquid products (green liquid petroleum gas ($C_{14} - C_{20}$), green jet fuel ($C_{11} - C_{13}$), and green diesel ($C_{13} - C_{14}$). A catalyst with high HDO ability would create a lot of green naphtha, whereas a catalyst with mild HDO ability would likely yield mostly green diesel (Júlia de Barros et al., 2020). Recent studies have reported the successful conversion of PFAD into renewable diesel through the HDO process utilising a fixed-bed flow reactor system using mesoporous catalysts (PtSn/20Al/SBA-15 and PtSn/ALPO-11 (Si/Al: 0) (Kim et al., 2021). Kim et al. (2021) further reported that high HDO activity owing to the large pore size, high acidity, and great metal dispersion on mesopores supported catalyst. Oh et al. (2018) findings align with Kim's discoveries, demonstrating that PtSn/20Al/SBA-15 and PtSn/ALPO-11 catalysts efficiently yield 63–66 % of diesel-rich (C_{16}, C_{18}) fuel. This is attributed to the presence of abundant rich acidic sites, including Lewis and Brønsted sites, which facilitate the favorable cleavage of C═O bonds through HDO and DO reactions. Former study by Gao et al. (2016) also discovered that high Si/Al favored C═O bond cleavage activity owing minimal acidity of the Zeolite Socony Mobil–5 (ZSM5). This occur due to fewer Al sites available in the ZSM5 framework when the Si/Al ratio increases (more silicon relative to aluminum). Indeed, the presence of abundant Lewis acid sites on ZSM5 facilitates the coordination of carbonyl groups, such as C═O, with these sites. This simultaneous interaction serves to reduce bond order while enhancing the HDO reaction (Corral-Pérez et al., 2019; Jonsson et al., 2021). Moreover, the acidic sites exhibits good linear correlation with the coke content and apparently Lewis acid sites may inhibit coking acitivity (Li et al., 2021).

ZSM5 is one of the most frequently used catalyst supports owing by recombination meso and microporous and rich Lewis acid sites characters (Gamliel et al., 2017). The ZSM5 is reported consist of 10-membered ring with a 3D channel with a diameter of 5.1–5.7 Å. Nevertheless, Hernandez's found that small pore diameter of ZSM5 limit the HDO reaction activity (Hernandez et al., 2016). Zeolite beta, in fact, has a larger pore diameter than ZSM5, displaying an average pore diameter falling within the 5.5–7.0 Å range. Furthermore, it can be effortlessly synthesised with a Si/Al ratio ranging from 12 to 200. However, the micropores strucure of the zeolite beta tends to collapse at high temperature (>600 °C) due to the dealumination process (Simancas et al., 2021). Remarkably, the incorporation of metal species into zeolite beta has been identified as the key factor contributing to its improved structural stability at high temperature.

Currently, utilization of inexpensive metals such as rare earth (RE) elements, i.e. La_2O_3, Nd_2O_3, and CeO_2, has recently gained interest in catalytic cracking process for the production of diesel-rich hydrocarbons (Rahimi and Karimzadeh, 2011). However, La's price is susceptible to fluctuations due to the impact of global supply chains. Indeed, the RE showed enhancement of catalyst stability by boosting the high temperature resistancy and high surface acid-basic sites (Escobar et al., 2019). This was affirmed by literature, in which the addition of La_2O_3 species with high acid-base character into zeolite Y not only improves the dispersion of active metal but also strengthens its thermal stability (Yu et al., 2021). Certainly, Li et al. (2021) corroborated that the inclusion of La not only aids in preserving the foundational structure of zeolite beta and ZSM5 but also significantly reduces its crystallinity. Incorporation of La species promote structure stability as La is an excellent sintering inhibitor agent. Furthermore, the presence of basic sites within La functions as a highly effective coke inhibitor, thereby restricting the catalyst deactivation due to coking during the HDO reaction (Zhang et al., 2009). La predominantly exhibit Lewis acid sites character, whereby the addition of high disperse of La into zeolite beta or ZSM5 will allow Lewis acid sites character of the La-containing catalyst to enhance significantly.

The majority of studies investigating the production of liquid hydrocarbons from various vegetable oils through catalytic HDO and deCOx (DCX and DCN) have underscored the importance of optimizing operational parameters to enhance hydrocarbon yield and diesel selectivity (Silva and de Andrade, 2021). Notably, reaction temperature exhibited most impactful factor on determining the hydrocarbon selectivity. Due to the endothermic nature of DCX and DCN, some researchers have observed that higher temperatures (T> 300 ℃) are preferred (Krobkrong et al., 2018). In the case of HDO, it was discovered that the HDO reaction is extremely exothermic in nature, by mean is unfavorable at high temperature (Baharudin et al., 2020). Ding et al. (2015), for instance, has succesfully obtained 100 % conversion and 92.2 % selectivity towards hexadecane over 5 % MoO_2/CNTs catalysts at a lower HDO temperature of 220 ℃. Note, H_2 atmopshere in HDO reaction also favours the formation of aliphatic hydrocarbon (7.6–92.2 %) which is generally less reactive than unsaturated ones. Therefore, it can ensure the stability of hydrocarbons, thereby optimizing the combustion ability of green diesel and producing a clean, non-sooty blue flame (Ding et al., 2015).

Based on aformentioned discussion, indeed, HDO still can be considered as an ideal process for production rich aliphatic hydrocarbons. Nevertheless, concerns about safety in HDO processes often arise. Hence, led to a continued reevaluation of the DO reaction by former studies. It is evident that a greater quantity of hydrocarbons (92 %) is attained through the DO reaction within 2 h under inert conditions (Safa-Gamal et al., 2021). Thongkumkoon et al. (2019), reported similar findings on DO of oleic acid, PFAD, refined palm stearin (RPS) and refined palm olein (RPO). Notably, although HDO and DO provide their own advantages, only a limited amount of research on palm by-product using RE metal catalyst was done using these two methods. Hence, the current study focuses on producing diesel-like fuel from HDO of PFAD over a La-modified zeolite-based catalyst. DO reaction was also carried out as comparison. The parametric study including the effects of reaction temperature (350–400 °C), catalyst loading (1–7 wt%), H_2 pressure (1–5 MPa), and reaction time (3–5 h) were carried out using OVAT. The

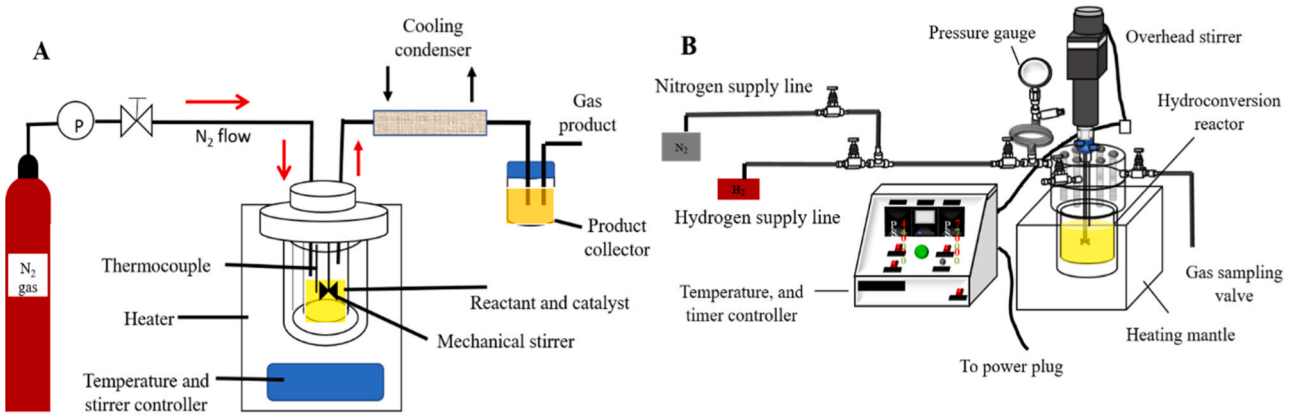

Fig. 1. Schematic diagram for (A) HDO and (B) DO reactors.

renewable diesel (RD 100) obtained was further evaluated for its fuel properties to observe its compatibility with petroleum diesel.

2. Experimental

2.1. Materials

The zeolite beta (SiO_2/Al_2O_3 = 38, SBET = 710 m^2g^{-1}) was purchased from Alfa Aeser in the United States. The R&M Company supplied lanthanum (III) nitrate hexahydrate with a purity exceeding 99 %. Standard solutions of alkanes and alkenes (C_8–C_{20}) and the internal standard 1-bromohexane with >98 % purity (GC grade) was purchased from Sigma Aldrich and utilised without further purification for gas chromatography (GC) analysis. For dilution, Merck (Germany) supplied N-Hexane (GC grade) with a purity of > 98 %. PFAD was obtained from Sime Darby Jomalina Sdn. Bhd. refinery, Teluk Panglima Garang, Selangor, Malaysia and used directly without any treatment. Acid content of the PFAD was evaluated using the AOCS Cd 3d-63 standard method. The PFAD was comprised of 55.2 % of saturated fatty acid and 46.4 % of unsaturated fatty acid with free fatty acid content of 84 %.

2.2. Synthesis of La-zeolite beta catalysts

The La-modified zeolite-based catalyst was prepared via the wet impregnation approach. 5 g of zeolite beta was initially impregnated with 10 wt% of the aqueous solution of metal salts described in Section 2.1. The mixture was then stirred for 4 h and dried at 100 ℃ for 24 h. The dried catalysts were then calcined at 500 °C for 4 h under atmosphere conditions at a heating rate of 10 °C min^{-1} before being reduced at 700 °C for 5 h using 5 vol% H_2 in argon at a heating rate of 2 °C min^{-1}. The catalysts were designated as La-zeolite beta (LZ). In the case of catalyst support, it will be denoted as zeolite beta.

2.3. Characterization of La-zeolite beta catalysts

The crystalline structure of catalysts was determined using XRD 6000 instrument (Shimadzu, Japan) in the range of 2θ = 5° - 80°. The crystallite size was calculated using the Debye–Scherrer equation at 2θ = 23°. TPD-CO_2 and NH_3 were utilised to measure the acidity and number of acidic/basic sites on the surface of catalysts. A quartz tube containing 0.05 g of sample was added to a thermal analyser (Thermo-Finnigan TPDRO 1100, USA), and the sample was prepared as reported elsewhere (Yan et al., 2018). Furthermore, a Bruker Tensor 27 FTIR spectrometer was employed to analyse the identity, structure, orientation, and bonding of NH_3 adsorption and desorption species on the catalyst surface. The output data from FTIR is presented by plotting the intensity (absorbance) as a function of the wavenumber or temperature (TPD-FTIR). The self-supporting wafer samples were prepared according to Yan et al. (2021b). The absorbance value was calculated following Eq. 1:

$$\text{Absorbance} = -\log \frac{(\text{Transmittance } 100\%)}{100} \quad (1)$$

Eventually, SEM equipped with an EDX analyser was used for observing the surface morphology and elemental compositions of the catalysts. Thereafter, the SEM connected to the Bruker X Flash 6I10 spectrometer for determining the elements like C, O, La, Si and Al present in the catalysts. The catalyst powder was initially dispersed on the aluminium sample holder covered by silver tape. Then, a thin layer of gold (Au) was used in coating the sample, representing a type of conducting material to avoid electric charging during the scanning process. The surface structure and morphology of the catalyst, underwent investigation under the electron microscope with a resolution of 3.5 nm. The instrument was operated at accelerating voltages of 20 kV and a current of 12 mA. TGA was applied to evaluate the thermo-stability of the catalyst using TGA, Mettler Toledo 990. The catalyst was heated under a 50 mL min^{-1} N_2 stream gradually to 900 °C at a rate of 30 °C min^{-1}.

2.4. Catalytic performance activity

The catalytic performance of PFAD over synthesized catalysts were conducted as illustrated in Fig. 1. In the case of HDO reaction, a total of 150 g of PFAD and 5 wt% of catalyst was mixed in a 600 mL high pressure, high-temperature reactor, the Novoclave type 3 (Buchi-glasuster, Switzerland) (Fig. 1 A). Prior to the reaction, the reactor was purged with N_2 at 40 °C for 10 minutes to produce an oxygen-free environment, then purged with pure H_2 for 10 minutes to create a complete H_2 environment, and the pressure of H_2 in the reactor was increased to 5.0 MPa. To obtain crude liquid product (CLP), the mixture was heated to 400 °C for 3 h while being agitated at 400 rpm. The CLP was distilled to obtain the refined crude product (RLP), which was purer and had a more attractive appearance for the industry besides could produced a qualified green diesel based on standard requirement. It is anticipated that extremely pure hydrocarbons would be produced (Cheng et al., 2019; Kiatkittipong et al., 2013). In contrast to HDO reaction, the DO of PFAD will be carried out in semi-batch reactor under N_2 atmosphere following method reported by Wan Khalit et al. (2022) (Fig. 1 B). The reactor was continuously stirred and flushed with inert N_2 gas for 3 h at a gradually increasing temperature of up to 350 °C. Finally, upon cooling at 20 °C, the vapour product was condensed with an external water cooler. GC-FID and GC-MS were used to analyse the collected liquid product from DO and RLP from HDO and GC-TCD for gas-phase analysis. A similar method was used for kinetic study, in which was investigated at three different temperatures (400 ℃, 420 ℃, and 450 ℃) for 1,2, 3, 4, 5 and 6 h of reaction. The catalyst's reusability

was assessed by simply washed the spent catalyst with methanol followed by dried overnight at 110 °C. The spent catalyst was reactivated by calcination and reduction of the catalyst as mentioned in Section 2.2.

2.5. Product analysis

The total acid number (TAN) of the liquid product was evaluated by employing the AOCS Cd 3d-63 standard, as shown in Eq. 2. The quantification of liquid products were analysed using an Agilent 7890 A series GC (USA) with FID and an HP-5 capillary column (dimension: 30 m inner diameter x 0.32 mm film) at 300 °C. The liquid products from HDO of guaiacol were analysed using an Agilent GC-6980 MS equipped with an Rtx-200 MS (30 m length, 0.25 mm ID, 0.5 μm film thickness) column. For quantification and the analysis of methanol, GC-FID was analysed using a 2014 Shimadzu GC, fitted with a Restek Stabilwax column (30 m, 0.32 mm ID with 1 μm film thickness). A GC-MS (Shimadzu QP2010 Plus) equipped with a Zebron ZB-5 MS column (dimension: 30 m × 0.25 mm × 0.25 m) was employed to separate the compounds in the CLP via the splitless inlet. The samples were first diluted with GC-grade hexane. The components of the spectra peaks were then identified according to the NIST database at 95 – 100 % similarity. Eq. 3 and Eq. 4 were employed to calculate product selectivity and hydrocarbon yield, respectively. Meanwhile, the yield of organic compounds (hydrocarbon fractions, alcohol) was calculated using Eq. 5.

$$\mathrm{TAN}(\%) = \frac{\mathrm{A} \times \mathrm{N} \times 56.11\ \mathrm{g\ mol-1}}{\mathrm{w}} \mathrm{x100} \quad (2)$$

A represents the KOH employed (mL), N is the normality of KOH, 56.11 g mol^{-1} is the molar mass of KOH, and w is the mass of the sample (g).

$$\mathrm{Gasoline}\Big/\mathrm{Diesel\ selectivity}(\%) = \frac{\mathrm{Hydrocarbon\ yield(C8-C12)/(C13-C18)}}{\mathrm{Total\ hydrocarbon\ in\ product\ (C8-C20)}} \mathrm{x100} \quad (3)$$

$$\mathrm{Hydrocarbon\ yield} = \frac{\mathrm{Total\ mole\ of\ n-alkane\ (C8-C20)\ in\ product\ \times 100}}{\mathrm{(Theoretical\ mole\ of\ HC\ in\ product)}} \quad (4)$$

$$\mathrm{Sproduct} = \frac{\mathrm{Cy}}{\Sigma \mathrm{ny}} \quad (5)$$

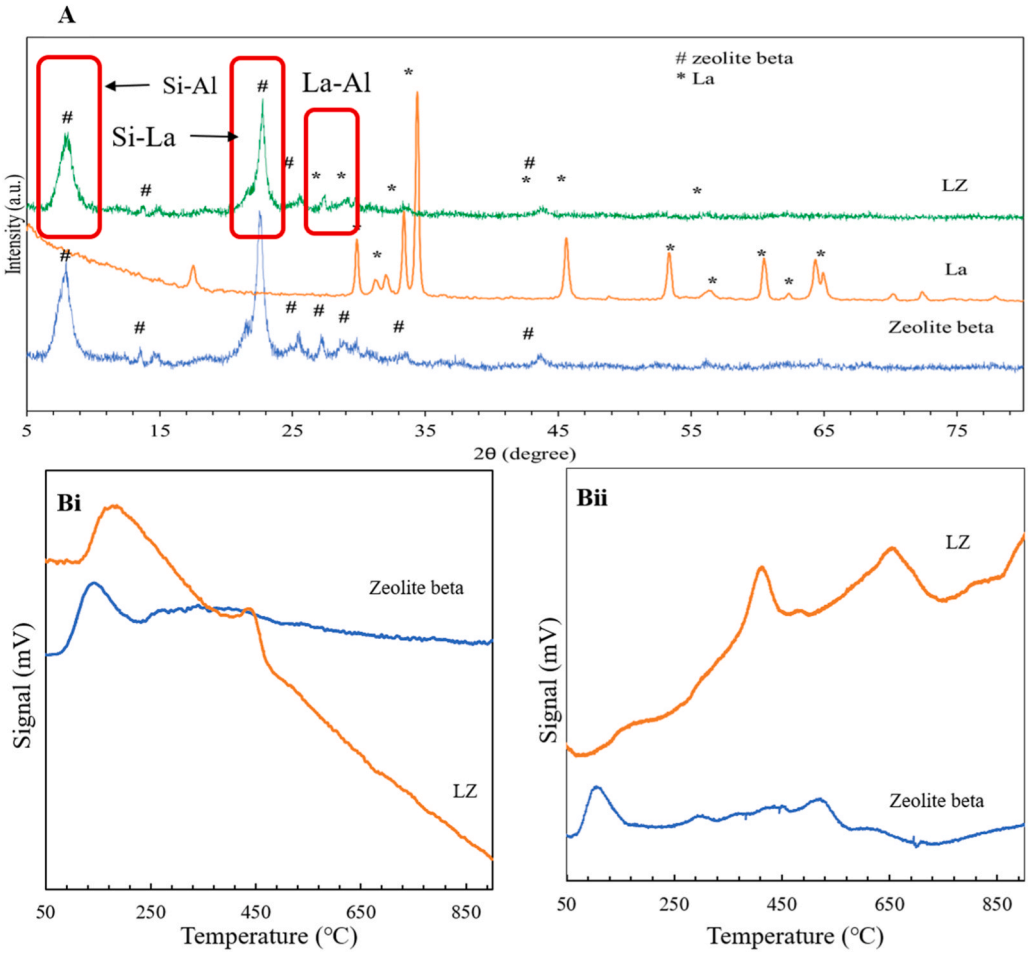

Fig. 2. A) XRD patterns for zeolite beta, La and LZ catalysts and Bi) TPD-NH_3 and Bii) TPD-CO_2 for zeolite beta and LZ.

Where Sproduct is the yield of organic compound (%), Cy represents the area of the desired organic compound, and ny is the total area of organic compounds.

The gaseous products collected were evaluated by the Agilent USA. Approximately, 2 mL of the collected gases were injected in an off-line GC (Agilent Model G1540N, USA) equipped with TCD to identify the type and concentration of gas produced during the DO and HDO reactions.

2.6. Fuel properties of renewable diesel from PFAD via HDO reaction

The RD 100 produced was further analysed using the method provided by the US biodiesel standard, which includes the TAN (AOCS Ca 5a − 40), kinematic viscosity (ASTM D445), density (ASTM D5002), calorific value (ASTM D 5865 − 0), and C, H, N, and S contents (ASTM D5373) using LECO CHN 628 and LECO S 628. The temperature and time of the combustion for CHN 628 ranged within 850–950 °C and 3 min, respectively, while the combustion analysis for S 628 was fixed within 2 min at 1350 °C. The concentration of oxygen (O) was calculated by subtracting 100 % to the sum of C, H, N and S.

3. Results and discussion

3.1. Catalyst characterization

Fig. 2A displays the XRD patterns for zeolite beta, La, and LZ. The crystalline phase of zeolite beta is confirmed by the strong diffraction peaks at 2θ = 7.8°, 14.6°, 22.6°, 25.3°, 27.1°, and 64.6° (JCPDS File No. 48 0038), while La is represented by 2θ = 17.7°, 29.8°, 34.4°, 45.5°, 53.3°, 60.7°, and 65.2° (JCPDS File No. 00–08–04). Interestingly, the introduction of La species to zeolite beta did not influence the XRD patterns, however, showed notable peaks associated with cubic metallic of lanthanum aluminium silicate at 2 = 26.1°, 29.2°, 30.1°, 39.7°, and 46.3° as well as highly crystalline characteristic peaks, attributed to the hexagonal La metallic phase at 2 = 29.4°, 31.2°, and 48.4° (JCPDS File No. 00–002–0618). JCPDS file No. 01–076–0642 resemblance to the parent zeolite, demonstrating that the distribution of La on zeolite beta is uniform. Sadek et al. (2020) suggested that modifications of the zeolite beta upon integration of an active metal indicate that the structure of the zeolites remains constant after loading the zeolite beta catalyst with various metals (Sadek et al., 2020).

The TPD patterns of the zeolite beta and LZ catalysts demonstrated that the NH_3 desorption peaks at T_{max} = 150 ℃ < 280 ℃ > 500 ℃ were associated with the presence of the weak, medium, and strong acid sites, respectively (Fig. 2Bi). Zeolite beta exhibited high amount of weak+medium acid sites (5909 μmol g^{-1}), followed by a strong acid site (2883 μmol g^{-1}) (Table 1). Conversely, LZ catalyst displayed a reduced weak+medium acid site (4700 μmol g^{-1}) and strong acid site (833 μmol g^{-1}) compared to zeolite beta. Evidently, the strong acid site corresponded to the Brønsted sites originated from the incorporation of Si-Al into the La framework, whilst the weak+medium acid sites were linked to the presence of Lewis acid types (Liu et al., 2013). Noted, the total acid sites (weak+medium and strong acid sites) dramatically decreased when La was added to zeolite beta, implying that the presence of the base characteristics of La contributed to the reduction of the acid sites (Abdulkareem-Alsultan et al., 2019). Previously, catalysts with weak, medium and strong acid sites were assumed to promote the DCX or DCN process through the C-O bond cleavages (Asikin-Mijan et al., 2020). Meanwhile, Botas et al. (2014) stated that the strong acid sites could have contributed to the excessive cracking and olefin oligomerisation, resulting in the generation of lighter hydrocarbon fractions and coke that lowered the HDO activities.

The basic sites were also detected in zeolite beta and LZ catalysts (Fig. 2 Bii). The weak, medium and strong basic sites are the main basis of active sites with variation dominant type of basic sites. However, it is noteworthy that the total amount of basic sites in both catalysts was 97 % lower than the total amount of acid sites, underscoring the dominance of acid sites as the primary active sites in zeolite beta. Nevertheless, the basic sites remained crucial for the oxygen elimination via the DCX pathway (Abdulkareem-Alsultan et al., 2020). It is worth noting that the LZ catalyst demonstrates a 38 % higher density of strong basic sites compared to zeolite beta, suggesting its dependency on La species for basicity. Furthermore, the abundant strong basic sites on the LZ catalyst position it as an effective coke inhibitor, enhancing catalyst stability while sustaining catalytic activity.

The IR spectra from the NH_3 adsorption on zeolite beta and LZ, respectively was illustrated in Figure S1. Both spectra reveal the presence of multiple major peaks between 1300 and 1600 cm^{-1}. The peak located at 1455 cm^{-1} was corresponded to the main vibrations of NH_4^+ ions produced by the protonation of NH_3 on Brønsted acid sites (Lónyi and Valyon, 2001). The band centred at approximately 1620 cm^{-1} was assigned to the symmetric bending vibrations of NH_3 coordinated on the Lewis acid sites (La, Al) (Yan et al., 2019). The remarkable decrease in the peak intensity of the LZ catalyst after addition of La species indicates the decreased bridging of Si(OH)Al groups due to the ion exchange between NH_4^+ and La^{3+}. This is due to the La^{3+} that eliminated a fraction of protons on the Al^{3+} sites, thus, lower the NH_4^+ vibration intensity at 1457 cm^{-1}, and consequently generated new La^{3+} Lewis acid sites (Yan et al., 2021a). Consequently, LZ was found to have fewer Brønsted and Lewis acid sites than the parent zeolite beta (Table 1), as evidence by the symmetric bending vibrations of NH_4^+ coordinated on La^{3+}. Reduced Brønsted and Lewis acid concentrations may be attributable to the blocking of acid sites on zeolite beta by La (Ma and Zhao, 2014). Furthermore, the presence of Lewis-bound NH_3 revealed that a portion of the metallic La sites were re-oxidized during wafer production, resulting in the formation of cationic La, which operated as a Lewis site (Yan et al., 2021a). Overall, the acid sites of LZ strongly relied on the acidity of zeolite beta, while the presence of basic sites originated from La_2O_3 (Yu et al., 2021).

Table 1 showed the surface area of LZ reduced from 648 to 556 m^2g^{-1} in comparison to the original zeolite. Reduction of surface area of LZ owing to the modification of the zeolite's structural caused by the introduction of lanthanum ions. This transformation may result in a partial collapse or reform of the zeolite framework which can decrease

Table 1
Physicochemical analysis of zeolite beta and LZ (Nur Azreena I. et al., 2021).

Catalysts	Surface area (m^2/g)	Pore volume (cm^3/g)	Pore size diameter (nm)	Acid strength (μmol g^{-1})[a]		Basic strength (μmol g^{-1})[b]		Total acid amount[c]	
				Weak + medium acid	Strong acid	Weak + medium basic	Strong basic	Brønsted acid	Lewis acid
Zeolite beta	648.0	0.22	2.03	5099	2883	158	90	598	119
LZ	556.4	0.29	2.09	4700	833	97	145	385	77

[a] Determined by TPD-NH_3 analysis.
[b] Determined by TPD-CO_2 analysis.
[c] Determined by FTIR-NH_3 analysis.

the overall surface area (Yu et al., 2021). The increase in pore diameter and volume (2.03–2.09 and 0.22–0.29, respectively) suggests that the introduction of lanthanum ions into the zeolite framework may have caused dealumination, that rearranged the Si/Al in the zeolite's structure through the elimination of aluminium atoms. This rearrangement create larger voids or mesopores as aluminum atoms are removed and replaced with larger lanthanum ions, thereby increasing the average pore diameter and pore volume if enough framework spaces are enlarged (Eschenbacher et al., 2021).

It worth nothing that both of zeolite beta and LZ exhibited pore size which is smaller than former reported active zeolite catalysts (usually within range of 5–20 nm)(Serrano et al., 2021; Sihombing et al., 2020). In the present study, the PFAD used apparently consist of long hydrocarbon chains fatty acid (C_{16} and $C_{18:1}$, see Section 2.1) with an average molecular weight of PFAD approximately 284.14 g/mol (Oo et al., 2022). Indeed, smaller pore size of zeolite beta and LZ (Table 1) and substantial size structure of PFAD may hinder its ability to penetrate the internal pores of zeolite. Hypothetically, it can be suggested that the majority of the reaction occurs on the surface of zeolite-based catalyst. interestingly, the inaccessibility of reactions within pores is not a concern, as the majority of active sites (metallic, acidic sites) synthesized in this study are typically located on the external surface of the zeolite particles (see SEM-EDX of LZ (Figure S2)) (Ghiaci et al., 2006). This assertion finds support in the studies by Zuo et al. (2013), who investigated the HDO of palm oil using Ni supported on nano-sized SAPO-11 catalysts. Despite the studied zeolite catalysts exhibiting smaller average pore diameters (2.0–2.3 nm), the HDO reaction was notably superior with hydrocarbon yield ~79 % and diesel selectivity ~53 %.

Fig. 3 A and 3 B show the surface morphology of the catalysts via SEM imaging. The zeolite beta showed an aggregates of regular cubic shape, while LZ appeared as uniform cubic crystals. The La were visible and well-distributed on the catalyst surface, yielding a La-rich condition. In addition, Fig. 3 C and 3 D display the Si, Al, and La contents on the surface of zeolite beta and LZ catalysts based on the EDX mapping. The uniform distribution of the La-rich region across the zeolite beta matrix was notable, which was ascribed to the La_2O_3 particles, and could have contributed to the high efficiency of the reactions. The EDX analysis also revealed that zeolite beta consisted of 2.5 wt% Al, 45.9 wt% Si, and 51.6 wt% O_2, whereas the LZ contained 1.7 wt% Al, 28.1 wt% Si, 56.0 wt% O_2, and 14.2 wt% La. Following the La loading, the increased O_2 was due to the formation of an oxide phase as a result of the oxygen-rich environment. Based on Table 1, the basic properties of LZ were highly affected by the oxygen-rich species (Ahmad et al., 2016). The presence of La elements on the LZ catalyst surface also implies that the La was successfully bound to the zeolite matrix.

3.2. Catalytic performance activity of PFAD via HDO reaction

The HDO of PFAD was carried out in the absence of catalyst (blank), zeolite beta, and LZ under the following reaction conditions: 5 wt% catalyst loading, 400 ℃ at H_2 pressure of 5 MPa for 3 h with a stirring speed of 400 rpm. Fig. 4 A depicts the hydrocarbon yield and selectivity profiles of the uncatalysed and catalysed products, respectively. Under a blank reaction, the hydrocarbon ($C_8 - C_{20}$) yield was not detected, while 57 – 75 % of hydrocarbons were obtained through catalysed reactions. Comparatively, LZ recorded a higher hydrocarbon yield than beta zeolite. This is associated with the large density of 4700 μmol g^{-1} of weak+medium acid sites (referred to as Lewis acid sites) and the low density of strong acid sites (referred to as Brønsted acid sites) at 833 μmol g^{-1}. Although beta zeolite demonstrated an 8 % increase in weak+medium acid sites, it's noteworthy that the density of strong acid sites was found to be 72 % greater than that of LZ. It's important to recognize that an excess density of strong acid sites is undesirable, as it inevitably promotes cracking activity, resulting in the formation of light hydrocarbons and volatile species. Indeed, zeolite beta catalysed reaction showed higher shorter chain hydrocarbon (C_8-C_{12}) (39 %) product than longer hydrocarbon ($C_{13} - C_{18}$) (36 %).

The PFAD was comprised of 55.2 % of saturated fatty acid and 46.4 % of unsaturated fatty acid (Section 2.1) and majorly composed of C_{16} (palmitic acid) and C_{18} (oleic acid) (Wan Khalit et al., 2022). Effective HDO PFAD typically yields hydrocarbons rich in C_{16} and C_{18} compounds, while DO will result in the production of C_{15} and C_{17} fractions (Wan Khalit et al., 2022). Based on Fig. 4B, eventhough LZ showed greater hydrocarbon yield (75 %) and diesel selectivity (55 %), yet minimal detection of C_{16} (2 %) and no detection of C_{18} compounds were observed (Kalai et al., 2017). Nevertheless, LZ produced major C_{15} and minor C_8-C_{11} (~42 %), suggesting that LZ also experienced C-O and

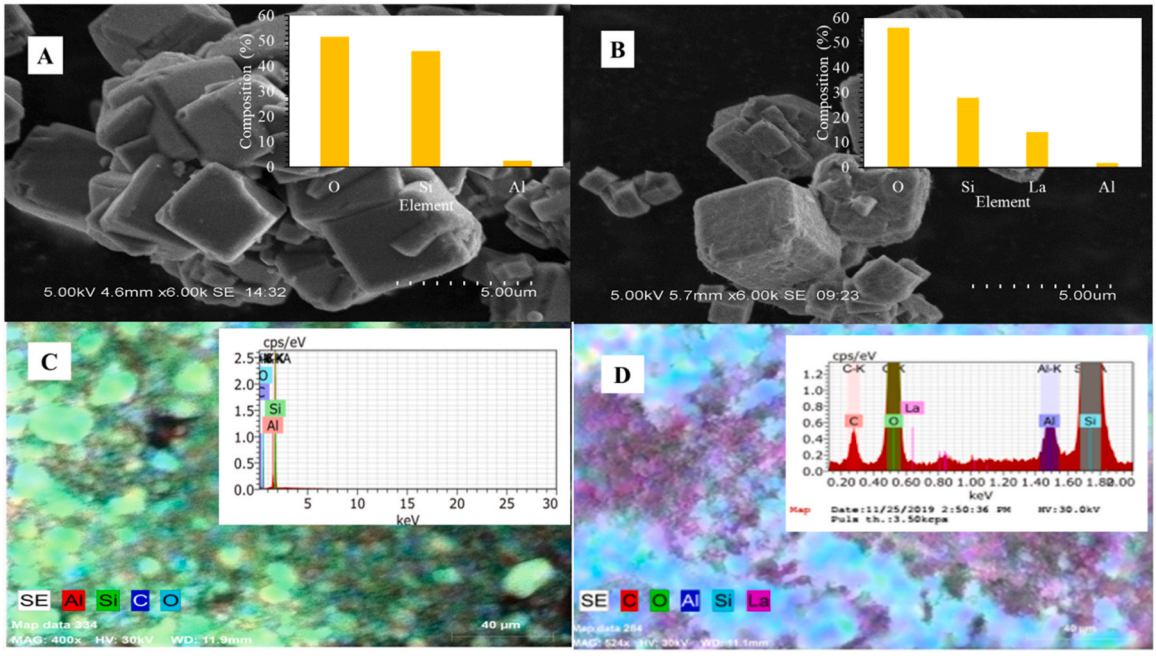

Fig. 3. A-D. SEM-EDX mapping and elemental analysis for zeolite beta and LZ.

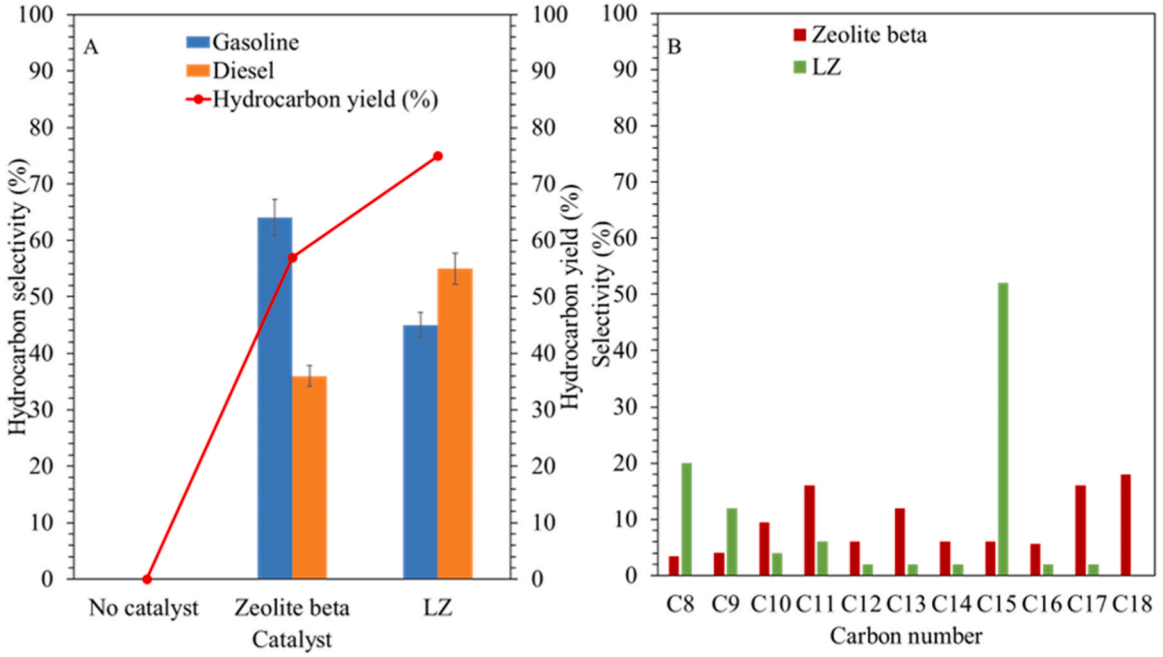

Fig. 4. A) Hydrocarbon yield and selectivity for HDO of PFAD and B) Carbon distribution of HDO of PFAD at 5 wt% of LZ loading, 400 ℃, 5 MPa of H_2 pressure for 3 h.

aggressive C−C bond cleavage via the deCOx and cracking reactions. Indeed, insignificant formation of HDO product by LZ catalysed reaction suggesting that the HDO product possibly undergoes cracking reaction forming shorter hydrocarbons. It's worth noting that C_{15} (52 %) was significantly more prevalent than C_{17}, which was found at only around 3 %. This suggests that LZ triggers aggressive DCX reactions that primarily target shorter-chain fatty acids over longer-chain ones (Baharudin et al., 2019).

Overall, LZ still superior than zeolite beta but the product selective toward DCX hydrocarbon, due to existence of rich weak+medium acid sites (4700 μmol g^{-1}). In the case of zeolite beta, although this catalyst exhibited higher weak+medium acid sites (5099 μmol g^{-1}), yet liquid

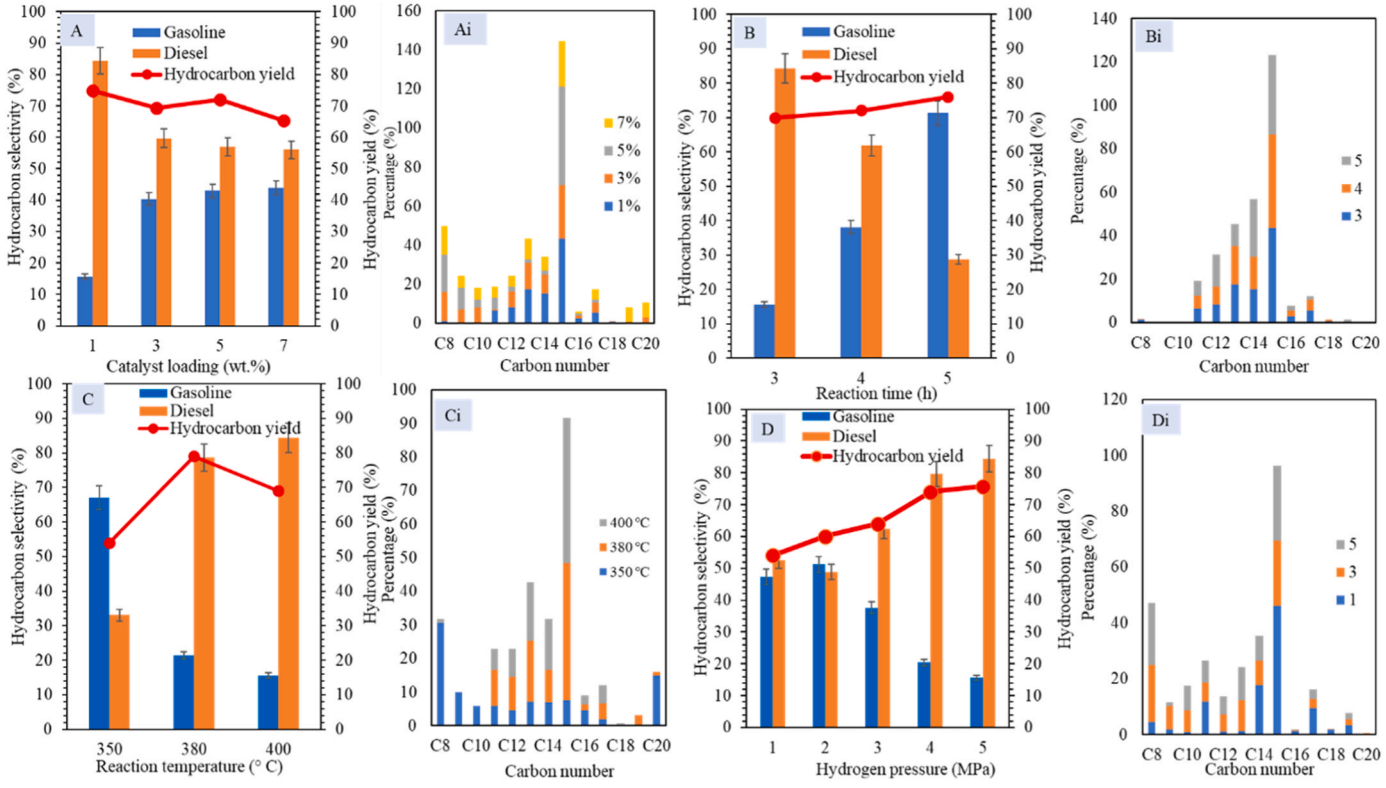

Fig. 5. A-D) Variety effect of catalyst loading, reaction time, reaction temperature and hydrogen pressure on the hydrocarbon selectivity HDO of PFAD, Ai-Di) Variety carbon distribution of HDO reaction for PFAD at different catalyst loading, reaction time, reaction temperature and hydrogen pressure.

product mainly results in wide distribution of hydrocarbon C_8-C_{18}, suggesting large strong acid (2883 μmol g^{-1}) on zeolite beta predominantly promote C-C bond cleavage than C-O bond cleavage. Nonetheless, zeolite beta demonstrated the presence of HDO product (C_{16}+C_{18}) (24 %) due higher acidity of zeolite beta than LZ which also beneficial in promoting the isomerization reactions of C_{16} and C_{18} than cracking reaction. Evidently, 1.3 % of -Cyclohexyldecane (C16H32) and 3-Methylheptadecane (C18H38) isomer species detected in the liquid product (see Figure S4).

3.3. Optimization of HDO reaction and its comparison with DO reaction

The optimal condition of LZ was determined using 5 wt% LZ loading at 400 ℃ and H_2 pressure of 5 MPa for 3 h. The optimisation study for the HDO of PFAD using LZ catalyst was investigated by OVAT approach (Abdulkareem-Alsultan et al., 2019) to determine the optimum balanced condition for all variables. This method offers the simplest implementation and primarily assists in the selection of significant parameters, including the amount of catalyst loading (1, 3, 5, and 7 wt%), reaction time (3 − 5 h), reaction temperature (350 − 400 °C), and H_2 pressure (1 − 5 MPa) that affect the hydrocarbon yield and selectivity.

The amount of catalyst showed a significant effect on the rate of HDO reaction, as well as the yield and selectivity of the desired products. Fig. 5 A depict the effects of different LZ loads (1 − 7 wt%) on the hydrocarbon yield and selectivity at 400 °C for 3 h under 5 MPa of H_2. The results showed that the HDO reaction (diesel selectivity) decreased proportionally from 84 % to 64 % as the catalyst loading was increased from 1 wt% to 7 wt% (Fig. 5 A) (Khan et al., 2020). The highest hydrocarbon yield and diesel selectivity of 75 % and 84 %, respectively, were recorded using 1 wt% catalyst loading. Meanwhile, the C_{15}-dominated diesel selectivity also increased as the catalyst loading increased from 1 wt% (43 %) to 3 wt% (51 %) (Fig. 5 Ai). The hydrocarbon yield decreased to 75 % and 65 % when the catalyst loading increased from 1 wt% to 7 wt%, respectively. This resulted in not only the decreased diesel selectivity containing C_{15} from 51 % to 23 % but also a higher hydrocarbon of C_{19} and C_{20} (~0.8 − 8 %) and lighter hydrocarbon (C_8 _ C_{12}; ~14 −19 %). In general, the overloading of the catalyst increased the possibility of undesirable side reactions, such as oligomerisation and C − C bond cleavage, which induced the formation of heavier hydrocarbons (Douvartzides et al., 2019). Therefore, 1 wt% catalyst loading was the most cost-effective option for the HDO reaction under the selected variables to produce the highest hydrocarbon yield and selectivity of C_{15}.

Fig. 5 B shows the effect of reaction time on the HDO reaction activity at 400 ℃, H_2 pressure of 5 MPa, and amount of catalyst loading at 1 wt% revealed that the hydrocarbon yield increased from 70 % to 76 % when the reaction time increased from 3 h to 5 h. Additionally, the maximum diesel selectivity was 84 % at 3 h of reaction time with the highest C_{15} (43 %). In contrast, the prolonged HDO reaction to 5 h resulted in a significant reduction in diesel selectivity from 84 % to 29 %, followed by the reduction of C_{15} from 36.4 % to 27.4 % (Fig. 5 Ci). Furthermore, C_8 − C_{10} (~1 − 17 %) was detected after 5 h of reaction time due to thermal cracking and unfavourable side reaction (such as polymerisation), which resulted in the lowest diesel selectivity. Based on the results, the HDO reaction was time-dependent as the diesel selectivity significantly changed when the reaction was prolonged. Overall, the optimal conditions for the catalytic activity of HDO of PFAD were determined at 400 °C using 1 wt%.

In Fig. 5 C, the rate of HDO activity based on the hydrocarbon yield increased with the increasing temperature from 350 °C (54 %) to 380 °C (79 %) but gradually decreased to 69 % when the reaction temperature was further increased to 400 °C. The trend was attributed to the high hydrocracking of hydrocarbons into volatiles species. Cracking and hydrogenation reactions take place concurrently in the hydrocracking process. The acid sites of the catalyst is required for isomerization and cracking activities while the metallic sites required for hydrogenation and dehydrogenation reactions (Wang et al., 2012). Correspondingly, the increasing reaction temperature from 350 to 400 °C significantly improved the diesel selectivity from 33 % to 84 %. According to Fig. 5 Bi, the C_{15} selectivity increased from 41 % to 43 % while C_{17} selectivity increased from 4.9 % to 5.2 % when the reaction temperature was increasd from 380 to 400 ℃ implied the more significant deCOx reaction in PFAD at higher reaction temperatures. Interestingly, the increased reaction temperature from 350 to 400 ℃ showed a lower amount of lighter hydrocarbon (C_8 − C_{10}), suggesting that the low amount of catalyst (1 wt%) containing mostly weak and medium acidity was unfavourable for thermal cracking at high reaction temperatures (Li et al., 2019). Overall, the recommended optimum reaction temperature was 400 °C for 3 h using 1 wt% LZ and H_2 pressure of 5 MPa.

When the H_2 pressure was varied at 1 − 5 MPa, the HDO of PFAD using LZ showed an increase in the hydrocarbon yield from 54 % to 76 % and diesel selectivity from 53 % to 84 %, while the gasoline selectivity decreased from 47 % to 16 % (Fig. 5 D). As shown in Fig. 5 Di, the liquid product consisted mostly of C_{15} (46 %), suggesting the occurrence of the deCOx reaction, which yielded C_{n-1} hydrocarbon products, as well as that the LZ catalyst promoted the C−O bond cleavage. Based on a previous study (Ding et al., 2015), a high H_2 pressure (5 MPa) improved the production of diesel range fuel and prevented undesirable cracking processes. Other studies have shown that the H_2 level influenced the catalyst reaction (Rozmysłowicz et al., 2012) and assists in maintaining the catalytic activity while reducing the coke formation (Yang et al., 2020). Furthermore, a significant number of cracking products (C_{11} – C_{14}) indicated an increased C – C bond cleavage. In short, the optimum H_2 pressure for the maximum hydrocarbon yield and selectivity of the HDO of PFAD was determined at H_2 pressure of 5 MPa, 400 ℃ using 1 wt% of LZ for 3 h.

3.4. DO of PFAD over zeolite beta and LZ catalyst under N2 atmosphere

Apart from that, the DO reaction of PFAD was conducted under N_2 atmosphere to observe the impact of the different reaction mediums on the catalytic activity of LZ at 350 °C, 5 wt% of zeolite beta and LZ within 2 h of reaction time (Figure S3). It shows that the hydrocarbon yield increased from 44 % to 86 % when LZ was introduced in N_2 DO, implying the occurrence of an improve catalytic DO reaction with the addition of La to the zeolite beta surface. When compared to the optimised H_2 pressure of the HDO reaction (5 MPa), the DO reaction showed a higher hydrocarbon yield (86 %) compared to the HDO reaction (76 %). Moreover, an increased hydrocarbon yield is observed at a high H_2 pressure of 5 MPa, suggesting that elevated pressures promote a greater extent of cracking (Di Vito Nolfi et al., 2021). N_2, on the other hand, prevented surface poisoning of La, thereby making metal sites more accessible for the DO reaction (Duan et al., 2019). Based on study by Asikin-Mijan et al., (2020), they mentioned that although DO does not involved H_2 for the hydrogenation step, the unsaturated hydrocarbon was still hydrogenated into saturated hydrocarbon involving the H_2 source from cracking or water-gas shift (WGS) (Eq. 6).

$$\text{Water-gas shift reaction} = CO{+}H_2O \leftrightharpoons CO_2{+}H_2 \quad (6)$$

Aforementioned study also claimed that the deoxygenated product (C15H30 and C17H34) also will undergo in-situ hydrogenation/dehydrogenation to produce $C_{15}H_{32}$ and $C_{17}H_{36}$. Assuming that PFAD is predominantly composed of C_{16} and $C_{18:1}$ fatty acid derivatives, and effective DO under a N_2 atmosphere will lead to the formation of hydrocarbons mainly comprised of C_{15} and C_{17}, along with by-products such as CO, CO_2, or H_2O (Lycourghiotis et al., 2021). It should be emphasised that since this reaction did not involve H_2, the H_2 source for hydrogenation might be supplied through cracking. The cracking could occur directly on the deoxygenated product leading light hydrocarbons. The occurrence of cracking reaction also in agreement with formation of cracking product such as C_{13} and C_{14} was detected in the DO reaction

using both catalysts, implying the occasional occurrence of the C − C cleavage. In fact, the addition of La to the zeolite beta enhanced the C − O bond cleavage, resulting in the generation of an exceptionally high-quality diesel fraction (Wan Khalit et al., 2020). The high C − O cleavage was in accordance with the high amount of weak and medium acid sites in LZ that led to the excellent DO activity and increased amount of the diesel fraction. Overall, the introduction of N_2 during LZ reaction resulted in a higher hydrocarbon yield (86 %) compared to H_2 (76 %) although the diesel selectivity was found to be equivalent (83 − 84 %). The findings showed that the reaction pathway was unaffected by neither H_2 nor non-H_2 environments, thus preserving the diesel selectivity.

3.5. Comparison of LZ catalyzed DO-diesel with purified LZ catalyzed HDO-diesel

Some compounds in the CLP, a non-purified HDO diesel indirectly promote undesirable qualities that potentially restricting their usage as transportation fuel. Therefore, additional processing, such as distillation is essential to obtain RLP with better physical and chemical properties or within limits specified by the regulatory agencies. Thus, in present study, the purification of CLP via the vacuum process was conducted to obtain the RLPs, which is also denoted as RD 100. In the purification process, the CLP further distillated within the distillation temperature 139–300 °C (Figure S5). The distillated liquid product further classified as "middle distillates (180–250 ℃)" and "lower distillate (< 180 ℃)" (Mancio et al., 2018).

Fig. 6A-B showed the comparison color for PFAD to the CLP, middle distillates (RD100) and DO product. Indeed, an immediate colour change from dark brown liquid (also reffered as CLP) (Fig. 6 Bii) to colourless (RD 100) (Fig. 6 Biii) was observed after post-purification. In contrast, the liquid product from the DO reaction was yellow in color (Fig. 6 Bi). The yellow color in the DO product is mostly caused by residual such as pigments, oxidation products, or trace elements that remain during the DO process and are present in the final product (Ruangudomsakul et al., 2021). Based on GCMS finding, the DO was composed of a mixture of gasoline (C_8 − C_{12}) and diesel hydrocarbon (C_{13} − C_{17}) fractions, while the RD 100 consisted of a greater variety of diesel hydrocarbon fractions (C_{13} − C_{15}) (Fig. 6 C i-iii).

Distillation process on CLP can be considered an effective approach for purification of the CLP into narrow range diesel fractions. This also supported by Fig. 6 C ii-iii and Figure S4 A, whereby the hydrocarbon fractions obtained in middle distillate product mainly comprise of hexadecane, C16H34 (73 %), followed by pentadecane, C15H32 (16 %). Hence, this finding confirming the middle distillate product is in exclusive diesel-ranged hydrocarbons. In short, the middles distillate obtained from CLP meet fuel quality like the RD 100. Noteworthy to mention, the result was also compared with the distillation curves of a petroleum diesel (Figure S5). The distillation temperature curve for RLP was higher than distillation curve petroleum diesel, indicated that the hydrocarbons in RLP may have higher molecular weights and boiling points compared to the hydrocarbons present in petroleum diesel, which is derived from crude oil through refining processes (Zhao et al., 2015). The curve has no plateau or flattening, indicating no azeotropic points in this temperature range. Azeotropic points result in a constant boiling point mixture when the vapor and liquid phases have the same composition at a given temperature and pressure. This implies that the separation of each fraction of the CLP is not hindered by the formation of constant boiling mixtures (Ohta et al., 2015). The yield of the middle distillates of CLP was 369 mL, while, the lower distillates obtained was 13.7 mL. No light naptha ranged below 100 ℃ and high distillates ranged > 300 ℃ containing heavy fractions yield were obtained. Indeed, the distillation residue boiling above 250 ℃ accounts for 30 % of the total mass and is solid at room temperature. This suggests that the distillation process used is suitable for separating the components with good efficiency.

Fig. 6 E illustrates the Van Krevelen diagram of the H/C and O/C atomic ratio of PFAD, CLP, and RD 100 obtained using LZ via the HDO and DO reactions. The result shows that the H/C and O/C atomic ratios of the PFAD were 0.5 and 0.3, respectively. Meanwhile, the H/C atomic ratio of the RD 100 and DO product were 0.5 and 1.9, respectively. In the case of O/C atomic ratio, all the catalysed products showed an O/C atomic ratio of 0.1 − 0.2, which was less than that of the PFAD feedstock at 0.3. According to the results, the oxygenates in PFAD were reduced

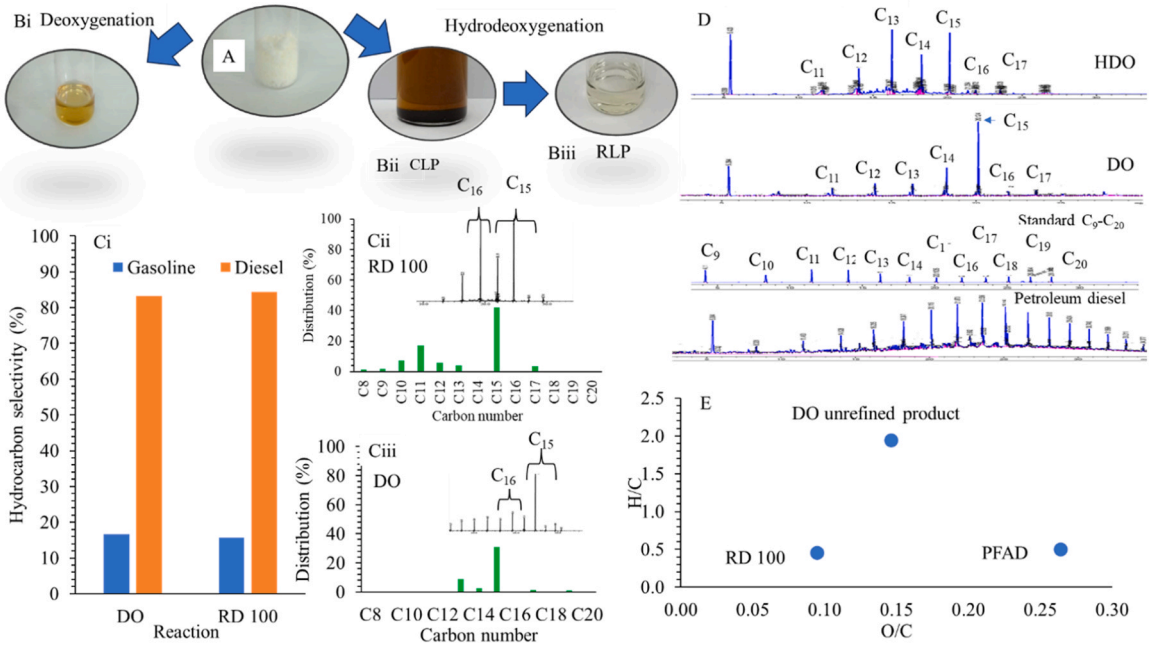

Fig. 6. A) PFAD as feedstock,Bi - Biii) DO, CLP and RD 100 liquid products, Ci - Ciii) Carbon distribution for DO and RD 100 liquid products, D) Chromatogram of RD 100, DO, standard C_8-C_{20} and petroleum diesel and E) H/C and O/C ratio for PFAD and liquid products obtained using LZ via HDO (RD 100) and DO unrefined product (Van Krevelen diagram).

almost entirely by the HDO. Indeed, in this investigation, HDO is far more preferred than DO. Similar trends also discovered by Ooi et al. (2019), whereby HDO exhibits remarkable advantages as high efficiency in removing oxygen atoms and maintaining the carbon number in the products. Indeed, the catalyst's efficacy in removing oxygenates is closely tied to its stability in a H_2 atmosphere. In this environment, H_2 plays a crucial role by hindering the adsorption of carbon on the catalyst's surface. Noted, H_2 prevent the deposition of carbonaceous species on the catalyst surface. H_2 competes with oxygenated compounds for adsorption sites on the catalyst, limiting the availability of reactive sites for carbon deposition (Dutta, 2020). Beside, in a H_2-rich atmosphere, carboxylic acids hydrogenate to form partially deoxygenated aldehyde intermediates and pure hydrocarbons and CO (Wai et al., 2022). However, since HDO is a hydrogen-intensive process, ensuring an adequate and consistent supply of H_2 can be challenging, especially on a large scale. In addition, handling of H_2 and operation at high pressures and temperatures pose safety risks that must be carefully managed.

3.6. Proposed reaction pathway

Based on the findings from GCFID, GC-MS and GCTCD (Fig. 5, Figure S4 and S6) the proposed reaction pathway for HDO of PFAD using LZ catalyst was established. Since PFAD is composed of 55.2 % saturated palmitic acid (C_{16}) and 46.4 % of unsaturated fatty acid majorly oleic acid (C18:1), possible reactions include HDO and hydrocracking or DCN and DCX occurred during the reaction were illustrated in Fig. 7. The products yielded from HDO reaction of PFAD catalyzed by LZ catalyst was tabulated in Table S1. It can be proposed that hexadecane (A1) is generated via hydrogenation (-H_2) and HDO of palmitic acid under a hydrogen-rich atmosphere, producing water as a by-product. Consequently, 38 % of saturated pentadecane ($C_{15}H_{32}$) (A2) was produced from DCX of hexadecane (-CO_2, H_2O) in A1 as can be referred to Table S1. In addition, a minor of undecane (C11H24), (0.43 %) was also produced from hydrocracking of hexadecane (A3).

Another potential pathway is through hydrogenation and HDO of oleic acid producing octadecane (C18H38) (B1). Meanwhile, the hydrocracking and DCN of oleic acid formed 7-tetradecene (C14H28) (B1) that consequently hydrogenated forming tetradecane ($C_{14}H_{30}$) (B2). In fact, it may also undergo cyclization forming cyclo-tetradecane (C14H28) (0.98 %) (B3). Additionally, the octadecane (C18H38) formed by hydrogenation and HDO of oleic acid was possibly hydrocracked and undergo DCN reaction to possibly produced undecane (C11H24), tridecane (C13H28) and hexadecane (C16H34) with CO as by-product. Additionally, the presence of lighter hydrocarbons (C_{10}, C_{11}, C_{12}, and C_{14}) demonstrated that the C − C bond could be broken into a short-chain hydrocarbon through cracking of the octadecane (See Fig. 7). During HDO reaction, the CO and H_2O will produce as a by-product under certain conditions. The CO produced from HDO reactions which is arises from secondary reactions such as WGS (Eq. 6) or Boudouard reactions (Eq. 7) (Silva and de Andrade, 2021). This fact was in agreement with GC-TCD analysis (Figure S6), whereby significant CO were detected in HDO reaction. For DO reaction, high CO species owing active occurrence of DCN reaction activity. In both reactions, notably, no detection of CO_2 was observed. In the case of the HDO reaction, the absence of CO_2 can be attributed to the high likelihood of reverse water-gas shift (RWGS) and Boudouard reactions, predominantly occurring due to the elevated reaction temperatures and pressures characteristic of the HDO process (Sonthalia and Kumar, 2017). In fact, the presence of desired HDO product (paraffinic hydrocarbon; hexadecane (C16H34)) further confirm the HDO reaction took placed. Indeed, the occurrences of DCX reaction in DO reaction is supported by formation of rich pentadecane (C15H32) (see Figure S4).

$$\text{Boudouard reaction} = 2CO \leftrightharpoons CO_2 + C \quad (7)$$

Based on Section 3.6, water can be produced via hydrogenation, HDO and DCN. Indeed, the presence of water in the reaction product can affect the catalyst acidity and, consequently, its reaction activity. Noted, the La_2O_3 exhibits hygroscopic behaviour when water molecules are adsorbed onto its molecular bonds and undergo a hydroxylation reaction that alters the molecular arrangement of La_2O_3 (Asikin-Mijan et al., 2015). This absorption causes La_2O_3 to be reduced to $La(OH)_3$. The hydroxyl group from $La(OH)_3$ can potentially reduce the original acidity of the LZ catalyst (Riza et al., 2020). The formation of $La(OH)_3$ was proved by the XRD patterns of the spent LZ catalyst which showed the presence of $La(OH)_3$ phases at 2θ = 22.4, 25.7, 27.1, 30.5, 35.3, 44.6 (JCPDS card No. 00–036–1481) (Figure S7). Although water molecules may inhibit acidity of catalyst, nevertheless, former studies on HDO discovered that the presence of water positively promote saturation of hydrocarbons forming rich alkanes hydrocarbons products via hydrogenation reaction (Badawi et al., 2011; Bettahar, 2020). Indeed, rich

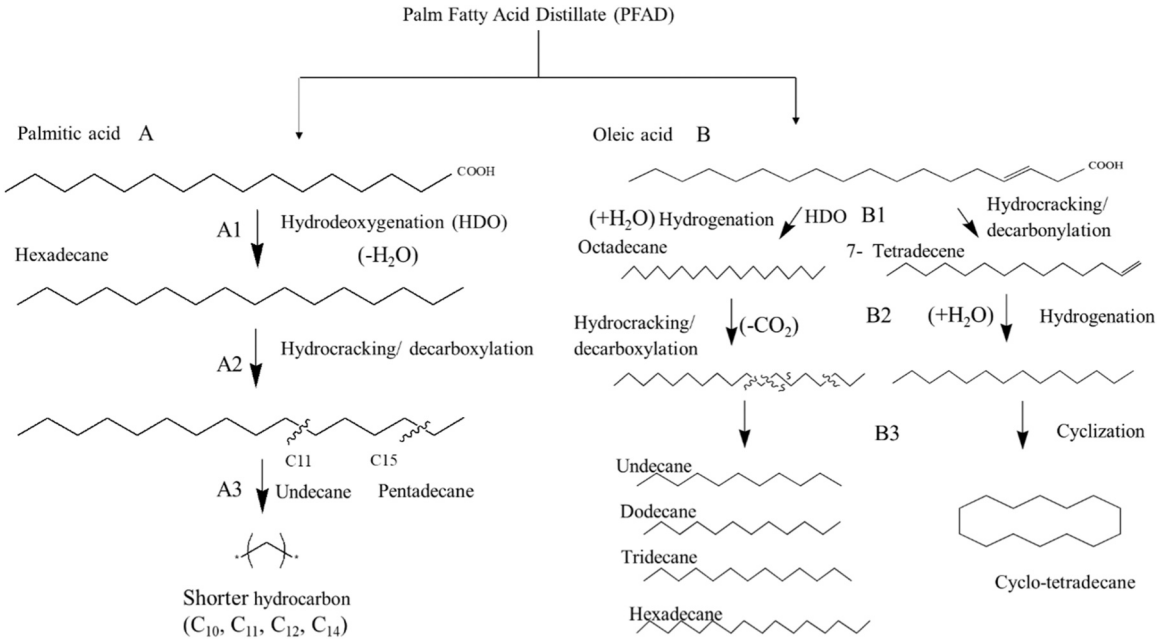

Fig. 7. Proposed HDO reaction pathway of PFAD.

alkanes species will increase cetane numbers of fuel and improve combustion efficiency and engine performance (Mancio et al., 2018). Notably, the use of alkane-rich fuel not only contributes to cleaner engine combustion but also enhances the efficiency of energy systems (Monteiro et al., 2022).

3.7. Kinetic study of HDO PFAD over LZ catalyst

Based on the greater oxygenated species elimination in RD 100 produced from HDO reaction, the details kinetic study for HDO of PFAD within 1 – 6 h reaction time and at temperatures within 400 – 440 °C using LZ were further investigated. It is recommended that the kinetic model of PFAD in hydrogen atmosphere follow the first order kinetic model with respect to the liquid phase components (Kumar et al., 2019). In this kinetic model, the rate of the reaction is assumed to be directly proportional to the concentration of the reactant. The first order kinetic model can be expressed as follows (Eq. 8);

$$\text{Rate} = \frac{-d[C_{HC}]}{dt} = k[C_{HC}] \tag{8}$$

Where k is the rate constant, t is reaction time, and $[C_{HC}]$ representing the concentration of hydrocarbon. In the kinetic study, the change in the hydrocarbon concentration with the time was following from the start of the reaction, $[C_{HC}]_0$ at t=0, to $[C_{HC}]_t$ at time t. Hence, the integration of rate law is as in Eq. 9:

$$\text{Ln}\frac{[C_{HC}]_t}{[C_{HC}]_0} = -kt \tag{9}$$

Therefore, the HDO of PFAD experimental results were plotted as a function of ln $[C_{HC}]_t/[C_{HC}]_0$ versus time, t (s) (Fig. 8a) for 1, 2, 3, 4, and 6 h at temperatures of 400, 420 and 440 ℃ (673, 693 and 713 K) and the rate constant was shown by the graph's slope (k). This graph showed a good agreement with Eq. 8 due to the acceptable value of the correlation coefficient (R^2>0.79), proves that the assumption made in this analysis was correct. In addition, the obtained graph was linear with increasing slopes, demonstrating that the HDO of PFAD was a first-order reaction, that provide evidence in favour of the hypothesis that the rate of the reaction is proportional to the reactant's concentration. The slopes of the graph of ln $[C_{HC}]_t$ versus time (t) were used to calculate the values of rate constants (k) for each reaction temperature, which were then tabulated in Table S2. It has been found that as the reaction temperature rises, the rate constant drops. This effect occurs due to an increase in temperature allows the reactant molecules to move more freely, leading them to catalyse the HDO reaction of PFAD more quickly (Hermida et al., 2016). This demonstrated that the temperature had a beneficial effect in speeding up the reaction rate but it also had an impact on the desired product.

The activation energy for the reaction could be calculated from the value of the rate constant, ks, using the Arrhenius equation (Eq.10). The Arrhenius equation is a relationship for the dependence of a reaction rate on temperature. It considers the activation energy (Ea), the pre-exponential factor (A), the universal gas constant (R), and the rate constant (ks) for chemical reactions at a given temperature (T). The activation energy refers to the minimum amount of energy needed to cause the molecular changes in a reactant (Duan et al., 2019).

$$\text{lnks} = \text{lnA} - \frac{-\text{Ea}}{\text{RT}} \tag{10}$$

$$\ln k = \frac{-Ea}{R}\left(\frac{1}{T}\right) + \ln A \tag{11}$$

The Arrhenius plot of ln k versus 1/T (Fig. 8B) was constructed by referring to Eq. 11, yielding a straight line from which the activation energy (Ea) and pre-exponential factor (A) could be calculated. A high correlation coefficient (R^2>0.90) for a straight line was found, demonstrating that the rate constant agrees with the Arrhenius equation. Indeed, the HDO of PFAD had an Ea of 144.4 kJ/mol, which is significantly lower than the previous study's value of 157 kJ/mol for the HDO of p-cresol to toluene (Duan et al., 2019) and 159 kJ/mol for HDO of stearic acid (Arora et al., 2019). This is to show that the catalyst used in this study is more active.

3.8. Reusability and stability of LZ catalyst

The reusability of the catalyst is important in determining the feasibility of large scale production of LZ catalyst. In this section, both

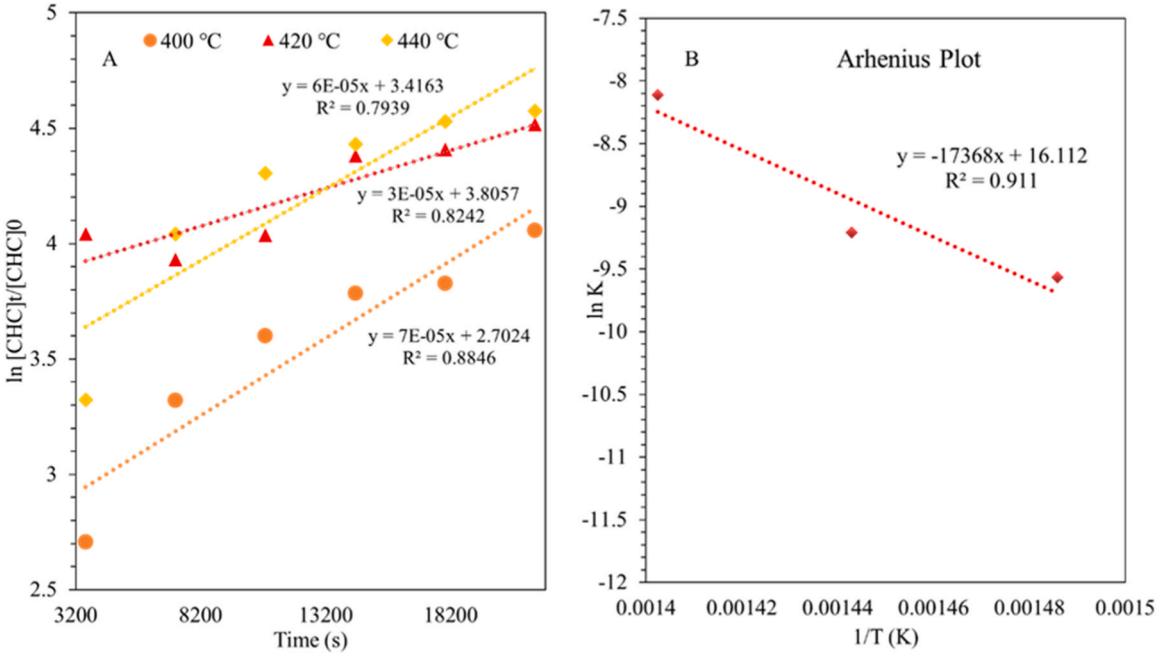

Fig. 8. A: Plot ln $[C_{HC}]_t/[C_{HC}]_0$ versus reaction time at various temperature for HDO of PFAD using LZ catalyst and 8 B: Arrhenius plot for HDO of PFAD using LZ catalyst.

reusability and stability study were discussed on both DO and HDO reaction to understand the catalyst durability and efficiency across different reaction types, aids in optimizing catalyst formulation for specific reactions. These findings are crucial for scaling up from laboratory to industrial applications, ensuring both economic viability and environmental sustainability. In this study, the HDO reaction was conducted for six consecutive runs. Between the first and sixth runs, there was a sharp decline in the hydrocarbon production and diesel selectivity (from 84 % to 29 %, and 76–21 % respectively) (Figure S8 Ai). The DO reaction on the other hands showed that the catalyst is active for five consecutive runs with decreasing trend of hydrocarbon yield from 67 % to 32 % and diesel selectivity of 55–31 % (Figure S8 Aii). It was believed that the catalyst's deactivation was the cause of the active sites decreasing in each subsequent run and the main cause of catalyst deactivation is coking (Camargo et al., 2020).

In fact, this observation aligns with the TGA (Figure S8) and EDX (Figure S9) analysis. TGA results depicted in Figure S8 Bi-ii, where both the spent LZ catalysts post-HDO and DO reactions yielded soft and hard coke residues. The 12 wt% of soft coke (T= 287–361 °C) and 7 wt% hard coke (T= 440–515 °C) were found in HDO reaction. Meanwhile for DO, both soft coke (T= 227–349 ℃) and hard coke (T= 397–529 ℃) were 10 %, respectively. This finding was in agreement with studies by Loe et al. (2019), Zhang et al. (2017). Among these cokes, hard coke residues tend to inhibit active sites (Abdulkareem-Alsultan et al., 2020), which tends to negatively affect the catalytic reaction activity. Nevertheless, when compared with former HDO and DO studies (Aliana-Nasharuddin et al., 2019; Hafriz et al., 2022), the average of hard coke form were 35 % lesser which suggests successful inhibition of LZ active site deactivation. Based on EDX results (Figure S9), only 6.2 % of carbon was found on the LZ-post HDO catalyst, while 12.9 % of carbon for LZ-post DO catalyst. Again formation of carbon affirmed TGA findings and its noteworthy that the utilization of H_2 reaction environment significantly reduce coking activity by 52 % when compared to the DO reaction. This underscores the advantageous nature of H_2 in the saturation process, effectively curbing polymerization reactions which lead to coke deposition (Zanuttini et al., 2015).

3.9. Comparison studies of different catalyst used for HDO and DO reactions

To summarize, Table 2 presents a detailed comparison between zeolite-based catalysts and industrial catalysts (NiMo and CoMo) in HDO reactions, revealing key factors influencing reaction activity. Indeed, former studies showed positive connection with effective HDO reaction activities with the presence of hydrogenating sites (metallic sites such as La, Al, Si, Ni and Co), Brønsted acid sites (weak+medium acid sites), total acid density, surface area, and synergistic interaction (Ameen et al., 2020; Aziz et al., 2023; Shim et al., 2015). Indeed, the present catalyst, LZ catalyst with rich weak+medium acid sites (4700 μmol/g) and larger surface area (556 m^2/g) showed similar trends with former studies. Interestingly, metallic species in LZ (La, Al and Si) and synergistic interaction of Si-Al (2θ=8.8°), Si-La (25.5°), La-Al (28.8°) (see Fig. 2A) existed on LZ catalyst also contributing to higher reaction activity leading rich diesel (C_{13}-C_{15}) product (84 %) (see Fig. 5). It should be noted that the LZ resulted in formation of rich HDO product (C16H34) (73 %) while the other studies HDO product within range of 17–25 % (Ameen et al., 2019; Shim et al., 2015), suggesting LZ has been shown to be effective in producing diesel like hydrocarbon fuel. In brief, most studies on catalytic HDO activity have concentrated on acid sites, but the role of basicity has remained limited. However, in our study, we found that the effectiveness of LZ is also tied to the presence of basic sites. Regarding pore size, although LZ had a smaller size (2.1 nm) compared to other catalysts (6–51 nm) (Ameen et al., 2019; Shim et al., 2015) but this factor alone didn't solely determine its effectiveness. Evidently, LZ consistently outperformed previous studies in HDO activity. Moreover, LZ displayed effective DO activity, resulting 86 % yield of DO products. This finding confirms LZ's effectiveness not only in an H_2 environment but also in a H_2-free reaction environment, showcasing its versatility and potential applicability across various reaction conditions.

3.10. Fuel properties of renewable diesel from PFAD

Table 3 compares the fuel properties of RD 100 produced by LZ via the HDO and DO reactions, including the TAN, density, kinematic viscosity, oxygen content, calorific value, and cetane index, to petroleum

Table 2
Comparison study of LZ, industrial and zeolite- based catalyst in HDO reaction.

Reaction	Feedstock	Catalyst	Metallic sites	Surface area (m^2/g)	Porosity (nm)	Acidity (μmol/g)		Basicity Acidity (μmol/g)	Main liquid product (%)	Reference
						Weak+medium (50–500 ℃)	Strong (>500 ℃)			
HDO	**Rubber seed oil**	Non-sulphided Ni-Mo/ γ-Al_2O_3	Ni, Mo, Al	77	6.3	6100	NA	NA	19 % (C_{15}) 17 % (C_{16}) 25 % (C_{17}) 12 % (C_{18}) HDO: 30 % DO: NA	(Ameen et al., 2020)
HDO	**Oleic acid**	CoMo	Co, Mo	4.24	50.6	NA	5870	NA	6 % (C_{17}) 12.% (Iso C_{17}) 8.6 % (C_9-C_{16}) HDO:34 % DO: NA	(Shim et al., 2015)
HDO	**PFAD**	Ni/Natural zeolite	Ni, Al, Si	155.4	1.9	2400	NA	NA	93 % (C_{15}-C_{18}) HDO: 84 % DO: NA	(Aziz et al., 2023)
HDO	**PFAD**	LZ	La	556.4	2.1	4700	1006	145	84 % (C_{13} – C_{15}) HDO:73 % (C_{16}) 57 % ($_{C15}$) DO: 86 %	This study

NA= Not available

Table 3
Fuel properties of renewable diesel from PFAD.

Fuel properties	ASTM Method[a]	HDO	DO	Petroleum diesel (ASTM D975-03)	Diesel ULSD[b]
TAN (%)	AOCS Ca 5a-40	1.8	3.4	-	-
Density at 15°C (g cm^{-3})	ASTM D5002	0.826	0.799	-	0.800–0.845
Kinematic viscosity at 40°C (mm^2 s^{-1})	ASTM D445	1.9	1.0	1.9–4.1	1.4–4.1
Oxygen content (%)	ASTM D5373	3.1	16.5	0	0
Calorific value (MJ kg^{-1})	ASTM D 5865–0	43.0	40.1	-	42.5
Cetane index	D 976	48	60	40	47–55

Test methods employed in this study.
[a] ASTM= American Society for Testing and Materials.
[b] ULSD= Ultra-low sulphur diesel.

diesel and Ultra-low Sulphur Diesel (ULSD). Since the presence of acidic species in the diesel has the potential to cause corrosion in the engine and storage facilities, the TAN value is an essential property of a renewable diesel that determines the amount of acid in the diesel based on the mass of KOH consumed to neutralise the acids in the fuels per gram of fuel. Table 3 shows that TAN decreased considerably to only 1.8 % from 84 %. The significant drop demonstrates that the majority of the fatty acids in the PFAD had been hydrodeoxygenated into hydrocarbon.

Furthermore, density is a critical fuel quality that directly affects engine performance (Graça et al., 2018). According to the findings, the density of RD 100 at 15 ℃ was 0.8260 g cm^{-3} (HDO) and 0.7999 g cm^{-3} (DO), which complied with the diesel ULSD standards (Recco et al., 2018). According to the results, the RD 100 would totally burned and thoroughly atomize, thus extending its service life (Peng, 2015). Meanwhile, viscosity is defined as the amount of internal friction between molecules or the barrier to liquid flow. Low fluid viscosity is required to minimise the ignition delay period (Pires et al., 2018). Based on the results, the kinematic viscosity of RD 100 was 1.9 mm^2 s^{-1} (HDO) and 1.0 mm^2 s^{-1} (DO), which is within the range of the petroleum diesel and ULSD specification standards. This indicates that RD 100 was a highly effective alternative fuel.

The calorific value of fuel indicates its energy content and efficiency. After the fuel is injected into the combustion chamber, its viscosity and density affect its atomisation and mixing with air (Aliana-Nasharuddin et al., 2019). Additionally, the presence of oxygen increased the viscosity of the fuel, whereas a greater proportion of hydrocarbons decreased the density (Sonthalia and Kumar, 2017). The analysis detected 3.1 % (HDO) and 5.5 % (DO) of oxygen, which could be related to the formation of oxygen-rich species, such as ketones, aldehydes, alcohols, and carboxylic acids. The result strongly correlated with the interaction of the gas phase (CO_2, CO) produced during DCX and DCN with the liquid product in a closed reaction system. Additionally, RD 100's calorific value was comparable to the ULSD standard at 43.0 MJ kg^{-1} (HDO) and 40 MJ kg^{-1} (DO) (42.5 MJ kg^{-1}).

The cetane index for RD100 was discovered to be 48 (HDO) and 60 (DO), which is comparable to the ULSD (47−55). This finding suggests that the RD100 (HDO) has a great ignition performance. It is believed that the RD100's exceptional cetane index is closely related to its incredibly high fraction of paraffinic fuel components (Sonthalia and Kumar, 2019). Furthermore, the HDO process using a LZ catalyst can efficiently remove oxygen from PFAD, producing hydrocarbons that closely resemble those derived from petroleum. This results in high-quality R100 that can be used in existing infrastructure and engines without modifications that can reduce capital expenditures. Previously, Phoon et al. (2017) also identified the high oxygenate compound content of diesel as a critical factor for excellent fuel combustion. In other words, the decrease in ignition delay and lower smoke level consequently increased the engine power. Thus, the quality of the produced RD 100 in this study was higher followed by the ULSD specification. Overall, the LZ-catalyzed hydrogen-assisted process represents a more promising techology for the oil and gas industry, where hydrogen is already used extensively in refining processes. In contrast, the emerging biorefinery industry confronts issues with H_2 supply due to its restricted availability and high cost. However, the emerging bioenergy sector may find it advantageous to invest in H_2 infrastructure, as it could considerably improve the efficiency of the process for the production of low-carbon fuel.

4. Conclusion

The study shows how LZ catalyst effectively converts PFAD into renewable diesel, offering a sustainable alternative to fossil fuels. The diesel obtained also helps in reducing carbon emissions, contributing to climate change mitigation. It was found that the HDO route was the preferred pathway for the conversion process due to the influence of the La-modified zeolite-based catalyst as an acid-base promoter. Principally, the HDO reaction using 1 wt% catalyst load at 400 °C under H_2 pressure of 5 MPa for 3 h of reaction time recorded the most significant hydrocarbon yield of approximately 75 % and diesel selectivity of 84 %. LZ catalysts were capable of performing six HDO and five DO cycles. However, HDO hydrocarbon production decreased from 84 % to 29 %, diesel selectivity from 76–21 %, and DO hydrocarbon yield from 67 % to 32 %, with diesel selectivity dropping from 55–31 %. Following the purification of the CLP in vacuum distillation at 139 − 300 °C, up to 84 % of hydrocarbon yield was obtained with a narrower diesel range (C_{13} − C_{15}, primarily C_{15}). The findings showed that the changes in the reaction pathways affected the selectivity of the products. Both HDO and DO reactions exhibited the considerable potential to produce renewable diesel under optimal reaction conditions. Specifically, both reaction pathways resulted from high concentration of weak+medium acid sites, as well as a hydrogen-rich environment for the HDO reaction, thereby enabling greater control over the diesel-fuel selectivity. In addition, the incorporation of hydrogen in HDO reaction led to a 52 % decrease in coking compared to DO reaction. This finding suggests that H_2 efficiently eliminates carbonaceous species from the surface of the LZ catalyst, thereby inhibiting the deposition of coke. Remarkably, the HDO reaction of C_{16} in PFAD produced RD 100 with abundant C_{16} hydrocarbons (73 %), while the DO reaction recorded a majority of C_{15} produced via the deCOx route. The quality of the RD 100 produced from PFAD via the HDO reaction were within the ULSD specification limits, indicating that the R100, a high-quality product, can be fitted into the existing infrastructure and engines without any modifications, or blended with regular diesel to significantly improve the fuel characteristics profile. Indeed, the high quality of R100 obtained from PFAD not only maintains customer acceptance but also contributes to realizing Malaysia's plan for promoting sustainable fuel. Overall, the LZ-catalyzed hydrogen-assisted process is a more promising technology for the oil and gas industry, where H_2 can be produced from various refinery feedstocks, hence, its implementation could significantly enhance efficiency and sustainability in refining operations. Conversely, the new biorefinery industry faces challenges with H_2 supply due to limited availability and high costs. Nevertheless, utilizing the LZ-catalyzed hydrogen-assisted process will not be an issue if biorefineries can improve their in-situ H_2 production process, thereby making it worthwhile for the emerging bioenergy sector.

Ethical approval

Not applicable

Funding

Not applicable

CRediT authorship contribution statement

I. Nur Azreena: Writing – original draft, Project administration, Methodology, Investigation, Formal analysis, Conceptualization. **N. Asikin-Mijan:** Writing – review & editing, Validation, Supervision. **H. L. N. Lau:** Supervision. **M.A. Hassan:** Supervision. **S. Mohd Izham:** Supervision. **E. Kennedy:** Supervision. **M. Stockenhuber:** Supervision. **P. Yan:** Supervision. **Y. H. Taufiq-Yap:** Writing – review & editing, Validation, Supervision.

Declaration of Competing Interest

The authors declare that they have no known competing financial interests or personal relationships that could have appeared to influence the work reported in this paper.

Data availability

The authors are unable or have chosen not to specify which data has been used.

Acknowledgement

The authors wish to thank the Director-General of Malaysian Palm Oil Board (MPOB) and Universiti Putra Malaysia for permission to publish this work.

Appendix A. Supporting information

Supplementary data associated with this article can be found in the online version at doi:10.1016/j.indcrop.2024.118907.

References

Abdulkareem-alsultan, Asikin Mijan, N., Mansir, N., Razali, S.Z., Yunus, R., Taufiq-Yap, Y.H., 2021. Combustion and emission performance of CO/NOx/SOxfor green diesel blends in a swirl burner. ACS Omega 6, 408–415. https://doi.org/10.1021/acsomega.0c04800.

Abdulkareem-Alsultan, G., Asikin-Mijan, N., Mansir, N., Lee, H.V., Zainal, Z., Islam, A., Taufiq-Yap, Y.H., 2019. Pyrolytic deoxygenation of waste cooking oil for green diesel production over Ag_2O_3 -La_2O_3/AC nano-catalyst. J. Anal. Appl. Pyrolysis 137, 171–184. https://doi.org/10.1016/j.jaap.2018.11.023.

Abdulkareem-Alsultan, G., Asikin-Mijan, N., Mustafa-Alsultan, G., Lee, H.V., Wilson, K., Taufiq-Yap, Y.H., 2020. Efficient deoxygenation of waste cooking oil over Co_3O_4-La_2O_3/ doped activated carbon for the production of diesel-like fuel. RSC Adv. 10, 4996–5009. https://doi.org/10.1039/c9ra09516k.

Ahmad, M., Farhana, R., Raman, A.A.A., Bhargava, S.K., 2016. Synthesis and activity evaluation of heterometallic nano oxides integrated ZSM-5 catalysts for palm oil cracking to produce biogasoline. Energy Convers. Manag. 119, 352–360. https://doi.org/10.1016/j.enconman.2016.04.069.

Aliana-Nasharuddin, N., Asikin-Mijan, N., Abdulkareem-Alsultan, G., Saiman, M.I., Alharthi, F.A., Alghamdi, A.A., Taufiq-Yap, Y.H., 2019. Production of green diesel from catalytic deoxygenation of chicken fat oil over a series binary metal oxide-supported MWCNTs. RSC Adv. 10, 626–642. https://doi.org/10.1039/c9ra08409f.

Ameen, M., Azizan, M.T., Ramli, A., Yusup, S., Abdullah, B., 2020. The effect of metal loading over Ni/γ-Al_2O_3 and Mo/γ-Al_2O_3 catalysts on reaction routes of hydrodeoxygenation of rubber seed oil for green diesel production. Catal. Today 355, 51–64. https://doi.org/10.1016/j.cattod.2019.03.028.

Ameen, M., Azizan, M.T., Yusup, S., Ramli, A., Yasir, M., Kaur, H., Wai, C.K., 2019. H-Y zeolite as hydrodeoxygenation catalyst for diesel range hydrocarbon production from rubber seed oil. Mater. Today Proc. 16, 1742–1749. https://doi.org/10.1016/j.matpr.2019.06.044.

Arora, P., Grennfelt, E.L., Olsson, L., Creaser, D., 2019. Kinetic study of hydrodeoxygenation of stearic acid as model compound for renewable oils. Chem. Eng. J. 364, 376–389. https://doi.org/10.1016/j.cej.2019.01.134.

Asikin-Mijan, N., Ooi, J.M.M., Abdulkareem-Alsultan, G., Lee, H.V., Mastuli, M.S., Mansir, N., Alharthi, F.A., Alghamdi, A.A., Taufiq-Yap, Y.H.H., 2020. Free-H_2 deoxygenation of Jatropha curcas oil into cleaner diesel-grade biofuel over coconut residue-derived activated carbon catalyst. J. Clean. Prod. 249, 119381 https://doi.org/10.1016/j.jclepro.2019.119381.

Asikin-Mijan, N., Taufiq-Yap, Y.H., Lee, H.V., 2015. Synthesis of clamshell derived Ca$(OH)_2$ nano-particles via simple surfactant-hydration treatment. Chem. Eng. J. 262, 1043–1051. https://doi.org/10.1016/j.cej.2014.10.069.

Aziz, I., Sugita, P., Darmawan, N., Dwiatmoko, A.A., 2023. Effect of desilication process on natural zeolite as Ni catalyst support on hydrodeoxygenation of palm fatty acid distillate (PFAD) into green diesel. South Afr. J. Chem. Eng. 45, 328–338. https://doi.org/10.1016/j.sajce.2023.07.002.

Aziz, I., Sugita, P., Darmawan, N., Dwiatmoko, A.A., Rustyawan, W., 2024. Hydrodeoxygenation of palm fatty acid distillate (PFAD) over natural zeolite-supported nickel phosphide catalyst: Insight into Ni/P effect. Case Stud. Chem. Environ. Eng. 9, 100571 https://doi.org/10.1016/j.cscee.2023.100571.

Badawi, M., Paul, J.F., Cristol, S., Payen, E., Romero, Y., Richard, F., Brunet, S., Lambert, D., Portier, X., Popov, A., Kondratieva, E., Goupil, J.M., El Fallah, J., Gilson, J.P., Mariey, L., Travert, A., Maugé, F., 2011. Effect of water on the stability of Mo and CoMo hydrodeoxygenation catalysts: a combined experimental and DFT study. J. Catal. 282, 155–164. https://doi.org/10.1016/j.jcat.2011.06.006.

Baharudin, K.B., Abdullah, N., Taufiq-Yap, Y.H., Derawi, D., 2020. Renewable diesel via solventless and hydrogen-free catalytic deoxygenation of palm fatty acid distillate. J. Clean. Prod. 274 https://doi.org/10.1016/j.jclepro.2020.122850.

Baharudin, K.B., Arumugam, M., Hunns, J., Lee, A.F., Mayes, E., Taufiq-Yap, Y.H., Wilson, K., Derawi, D., 2019. Octanoic acid hydrodeoxygenation over bifunctional Ni/Al-SBA-15 catalysts. Catal. Sci. Technol. 9, 6673–6680. https://doi.org/10.1039/c9cy01710k.

Bettahar, M.M., 2020. The hydrogen spillover effect. A misunderstanding story. Catal. Rev. - Sci. Eng. 1–39. https://doi.org/10.1080/01614940.2020.1787771.

Botas, J.A., Serrano, D.P., García, A., Ramos, R., 2014. Catalytic conversion of rapeseed oil for the production of raw chemicals, fuels and carbon nanotubes over Ni-modified nanocrystalline and hierarchical ZSM-5. Appl. Catal. B Environ. 145, 205–215. https://doi.org/10.1016/j.apcatb.2012.12.023.

Camargo, M., de, O., Castagnari Willimann Pimenta, J.L., de Oliveira Camargo, M., Arroyo, P.A., 2020. Green diesel production by solvent-free deoxygenation of oleic acid over nickel phosphide bifunctional catalysts: effect of the support. Fuel 281, 118719. https://doi.org/10.1016/j.fuel.2020.118719.

Cheng, J., Zhang, Z., Zhang, X., Liu, J., Zhou, J., Cen, K., 2019. Hydrodeoxygenation and hydrocracking of microalgae biodiesel to produce jet biofuel over $H_3PW_{12}O_{40}$-Ni/hierarchical mesoporous zeolite Y catalyst. Fuel 245, 384–391. https://doi.org/10.1016/j.fuel.2019.02.062.

Corral-Pérez, J.J., Copéret, C., Urakawa, A., 2019. Lewis acidic supports promote the selective hydrogenation of carbon dioxide to methyl formate in the presence of methanol over Ag catalysts. J. Catal. 380, 153–160. https://doi.org/10.1016/j.jcat.2019.10.013.

Di Vito Nolfi, G., Gallucci, K., Rossi, L., 2021. Green diesel production by catalytic hydrodeoxygenation of vegetables oils. Int. J. Environ. Res. Public Health 18. https://doi.org/10.3390/ijerph182413041.

Ding, R., Wu, Y., Chen, Y., Liang, J., Liu, J., Yang, M., 2015. Effective hydrodeoxygenation of palmitic acid to diesel-like hydrocarbons over MoO_2/CNTs catalyst. Chem. Eng. Sci. 135, 517–525. https://doi.org/10.1016/j.ces.2014.10.024.

Douvartzides, S.L., Charisiou, N.D., Papageridis, K.N., Goula, M.A., 2019. Green diesel: Biomass feedstocks, production technologies, catalytic research, fuel properties and performance in compression ignition internal combustion engines. Energies 12. https://doi.org/10.3390/en12050809.

Duan, H., Liu, J.C., Xu, M., Zhao, Y., Ma, X.L., Dong, J., Zheng, X., Zheng, J., Allen, C.S., Danaie, M., Peng, Y.K., Issariyakul, T., Chen, D., Kirkland, A.I., Buffet, J.C., Li, J., Tsang, S.C.E., O'Hare, D., 2019. Molecular nitrogen promotes catalytic hydrodeoxygenation. Nat. Catal. 2, 1078–1087. https://doi.org/10.1038/s41929-019-0368-6.

Dutta, S., 2020. Hydro(deoxygenation) reaction network of lignocellulosic oxygenates. ChemSusChem 13, 2894–2915. https://doi.org/10.1002/cssc.202000247.

Eschenbacher, A., Andersen, J.A., Jensen, A.D., 2021. Catalytic conversion of acetol over HZSM-5 catalysts – influence of Si/Al ratio and introduction of mesoporosity. Catal. Today 365, 301–309. https://doi.org/10.1016/j.cattod.2020.03.041.

Escobar, J., Barrera, M.C., Valente, jaime S., Solis-Casados, D.A., Santes, V., Terrazas, J. E., Fouconnier, B.A.R., 2019. Dibenzothiophene hydrodesulfurization over P-CoMo on sol-gel alumina modified by La addition. Effect of rare-earth content. Catalysts 9, 1–20.

Gamliel, D.P., Baillie, B.P., Augustine, E., Hall, J., Bollas, G.M., Valla, J.A., 2017. Nickel impregnated mesoporous USY zeolites for hydrodeoxygenation of anisole David. Microporous Mesoporous Mater. https://doi.org/10.1016/j.micromeso.2017.10.027.

Gao, Y., Zheng, B., Wu, G., Ma, F., Liu, C., 2016. Effect of the Si/Al ratio on the performance of hierarchical ZSM-5 zeolites for methanol aromatization. R. Soc. Chem. 1–3. https://doi.org/10.1039/C6RA17084F.

Ghiaci, M., Abbaspur, A., Kalbasi, R.J., 2006. Internal versus external surface active sites in ZSM-5 zeolite: part 1. Fries rearrangement catalyzed by modified and unmodified H3PO 4/ZSM-5. Appl. Catal. A Gen. 298, 32–39. https://doi.org/10.1016/j.apcata.2005.09.015.

Graça, I., Bacariza, M.C., Fernandes, A., Chadwick, D., 2018. Desilicated NaY zeolites impregnated with magnesium as catalysts for glucose isomerisation into fructose. Appl. Catal. B Environ. 224, 660–670. https://doi.org/10.1016/j.apcatb.2017.11.009.

Hafriz, R.S.R.M., Nor Shafizah, I., Arifin, N.A., Maisarah, A.H., Salmiaton, A., Shamsuddin, A.H., 2022. Comparative, reusability and regeneration study of potassium oxide-based catalyst in deoxygenation reaction of WCO. Energy Convers. Manag. X 13, 100173. https://doi.org/10.1016/j.ecmx.2021.100173.

Han, J., Duan, J., Chen, P., Lou, H., Zheng, X., Hong, H., 2011. Nanostructured molybdenum carbides supported on carbon nanotubes as efficient catalysts for one-

step hydrodeoxygenation and isomerization of vegetable oils. Green. Chem. 13, 2561–2568. https://doi.org/10.1039/c1gc15421d.
Hermida, L., Amani, H., Abdullah, A.Z., Mohamed, A.R., 2016. Deoxygenation of palmitic acid to produce diesel-like hydrocarbons over nickel incorporated cellular foam catalyst: a kinetic study. J. Adv. Chem. Eng. 6, 1–8. https://doi.org/10.4172/2090-4568.1000144.
Hernandez, M.A., Abbaspourrad, A., Petranovskii, V., Rojas, F., Portillo, R., Salgado, M. A., Hernandez, G., Velazco, M., de los, A., Ayala, Ed, Quiroz, Ka.F., 2016. Estimation of nanoporosity of ZSM-5 zeolites as hierarchical materials. Intech 11, 13.
Jonsson, R., Ho, P.H., Wang, A., Skoglundh, M., Olsson, L., 2021. The impact of lanthanum and zeolite structure on hydrocarbon storage. Catalysts 11. https://doi.org/10.3390/catal11050635.
Júlia de Barros, D.M., Bastos de Rezende, D., Márcia Duarte Pasa, V., 2020. Deoxygenation of Macauba acid oil over Co-based catalyst supported on activated biochar from Macauba endocarp: a potential and sustainable route for green diesel and biokerosene production. Fuel 269, 117253. https://doi.org/10.1016/j.fuel.2020.117253.
Kalai, D.Y., Stangeland, K., Li, H., Yu, Z., 2017. The effect of La on the hydrotalcite derived Ni catalysts for dry reforming of methane. Energy Procedia 142, 3721–3726. https://doi.org/10.1016/j.egypro.2017.12.267.
Khan, S., Fazly Abdul Patah, M., Mohd Ashri Wan Daud, W., 2020. Synergistic effect with and without Ni metal over ZSM-5/SAPO-11 catalyst in hydrodeoxygenation of palm oil. IOP Conf. Ser. Mater. Sci. Eng. 778 https://doi.org/10.1088/1757-899X/778/1/012068.
Kiatkittipong, W., Phimsen, S., Kiatkittipong, K., Wongsakulphasatch, S., Laosiripojana, N., Assabumrungrat, S., 2013. Diesel-like hydrocarbon production from hydroprocessing of relevant refining palm oil. Fuel Process. Technol. 116, 16–26. https://doi.org/10.1016/j.fuproc.2013.04.018.
Kim, K., Higai, D., Hou, X., Peng, M., Qian, E.W., 2021. Production of normal paraffins with an even carbon number via selective hydrodeoxygenation of palm fatty acid distillate over Pt-Sn catalysts. Ind. Eng. Chem. Res. 60, 2881–2889. https://doi.org/10.1021/acs.iecr.0c05922.
Krobkrong, N., Itthibenchapong, V., Khongpracha, P., Faungnawakij, K., 2018. Deoxygenation of oleic acid under an inert atmosphere using molybdenum oxide-based catalysts. Energy Convers. Manag. 167, 1–8. https://doi.org/10.1016/j.enconman.2018.04.079.
Kumar, P., Maity, S.K., Shee, D., 2019. Role of NiMo alloy and Ni species in the performance of NiMo/alumina catalysts for hydrodeoxygenation of stearic acid: a kinetic study. ACS Omega 4, 2833–2843. https://doi.org/10.1021/acsomega.8b03592.
Lam, J.E., Mohamed, A.R., Kay Lup, A.N., Koh, M.K., 2022. Palm fatty acid distillate derived biofuels via deoxygenation: properties, catalysts and processes. Fuel Process. Technol. 236, 107394 https://doi.org/10.1016/j.fuproc.2022.107394.
Li, Y., Sun, D., Zhao, X., Yamada, Y., Sato, S., 2021. Control of coke deposition in solid acid catalysis through the doping of transition metal combined with the assistance of H2: a review. Appl. Catal. A Gen. 626, 118340 https://doi.org/10.1016/j.apcata.2021.118340.
Li, M., Xing, S., Yang, L., Fu, J., Lv, P., Wang, Z., Yuan, Z., 2019. Nickel-loaded ZSM-5 Catalysed Hydrogenation of Oleic Acid: the game between acid sites and metal centres. Appl. Catal. A Gen. 587, 117112 https://doi.org/10.1016/j.apcata.2019.117112.
Liu, Q., Zuo, H., Wang, T., Ma, L., Zhang, Q., 2013. One-step hydrodeoxygenation of palm oil to isomerized hydrocarbon fuels over Ni supported on nano-sized SAPO-11 catalysts. Appl. Catal. A Gen. 468, 68–74. https://doi.org/10.1016/j.apcata.2013.08.009.
Loe, R., Huff, K., Walli, M., Morgan, T., Qian, D., Pace, R., Song, Y., Isaacs, M., Santillan-Jimenez, E., Crocker, M., 2019. Effect of Pt promotion on the Ni-catalyzed deoxygenation of tristearin to fuel-like hydrocarbons. Catalysts 9. https://doi.org/10.3390/catal9020200.
Lónyi, F., Valyon, J., 2001. A TPD and IR study of the surface species formed from ammonia on zeolite H-ZSM-5, H-mordenite and H-beta. Thermochim. Acta 373, 53–57. https://doi.org/10.1016/S0040-6031(01)00458-0.
Lycourghiotis, S., Kordouli, E., Kordulis, C., Bourikas, K., 2021. Transformation of residual fatty raw materials into third generation green diesel over a nickel catalyst supported on mineral palygorskite. Renew. Energy 180, 773–786. https://doi.org/10.1016/j.renene.2021.08.059.
Ma, Bing, Zhao, Chen, 2014. High grade diesel production from hydrodeoxygenation of palm oil over hierarchically structured Ni/HBEA catalyst. Green. Chem. 17, 1692–1701. https://doi.org/10.1039/b000000x.
Mailaram, S., Maity, S.K., 2019. Techno-economic evaluation of two alternative processes for production of green diesel from karanja oil: a pinch analysis approach. J. Renew. Sustain. Energy 11. https://doi.org/10.1063/1.5078567.
Mancio, A.A., da Mota, S.A.P., Ferreira, C.C., Carvalho, T.U.S., Neto, O.S., Zamian, J.R., Araújo, M.E., Borges, L.E.P., Machado, N.T., 2018. Separation and characterization of biofuels in the jet fuel and diesel fuel ranges by fractional distillation of organic liquid products. Fuel 215, 212–225. https://doi.org/10.1016/j.fuel.2017.11.029.
Monteiro, R.R.C., dos Santos, I.A., Arcanjo, M.R.A., Cavalcante, C.L., de Luna, F.M.T., Fernandez-Lafuente, R., Vieira, R.S., 2022. Production of jet biofuels by catalytic hydroprocessing of esters and fatty acids: a review. Catalysts 12, 237. https://doi.org/10.3390/catal12020237.
Nur Azreena, I., Lau, H.L.N., Asikin-Mijan, N., Hassan, M.A., Izham, S.M., Kennedy, E., Stockenhuber, M., Mastuli, M.S., Alharthi, F.A., Alghamdi, A.A., Taufiq-Yap, Y.H., 2021. A promoter effect on hydrodeoxygenation reactions of oleic acid by zeolite beta catalysts. J. Anal. Appl. Pyrolysis 155, 105044. https://doi.org/10.1016/j.jaap.2021.105044.
Oh, Y.K., Hwang, K.R., Kim, C., Kim, J.R., Lee, J.S., 2018. Recent developments and key barriers to advanced biofuels: a short review. Bioresour. Technol. 257, 320–333. https://doi.org/10.1016/j.biortech.2018.02.089.
Ohta, H., Yamamoto, K., Hayashi, M., Hamasaka, G., Uozumi, Y., Watanabe, Y., 2015. Low temperature hydrodeoxygenation of phenols under ambient hydrogen pressure to form cyclohexanes catalysed by Pt nanoparticles supported on H-ZSM-5. Chem. Commun. 51, 17000–17003. https://doi.org/10.1039/c5cc05607a.
Oo, Y.M., Prasit, T., Thawornprasert, J., Somnuk, K., 2022. Continuous double-step esterification production of palm fatty acid distillate methyl ester using ultrasonic tubular reactor. ACS Omega 7, 14666–14677. https://doi.org/10.1021/acsomega.1c07230.
Ooi, X.Y., Gao, W., Ong, H.C., Lee, H.V., Juan, J.C., Chen, W.H., Lee, K.T., 2019. Overview on catalytic deoxygenation for biofuel synthesis using metal oxide supported catalysts. Renew. Sustain. Energy Rev. 112, 834–852. https://doi.org/10.1016/j.rser.2019.06.031.
Peng, D.X., 2015. Exhaust emission characteristics of various types of biofuels. Adv. Mech. Eng. 7, 1–7. https://doi.org/10.1177/1687814015593036.
Phoon, L.Y., Mustaffa, A.A., Hashim, H., Mat, R., Yee, L., Mustaffa, A.A., Hashim, H., Mat, R., Phoon, L.Y., Mustaffa, A.A., Hashim, H., Mat, R., 2017. Performance and emission characteristics of green diesel blends containing diethyl-succinate and 1-octanol. Chem. Eng. Trans. 56, 889–894. https://doi.org/10.3303/CET1756149.
Pires, A.P.P., Han, Y., Kramlich, J., Garcia-Perez, M., 2018. Chemical composition and fuel properties of alternative jet fuels. BioResources 13, 2632–2657. https://doi.org/10.15376/biores.13.2.2632-2657.
Rahimi, N., Karimzadeh, R., 2011. Catalytic cracking of hydrocarbons over modified ZSM-5 zeolites to produce light olefins: a review. Appl. Catal. A Gen. 398, 1–17. https://doi.org/10.1016/j.apcata.2011.03.009.
Recco, E., Mayorga, M.A., Cadavid, J.G., Yesid, O., Palacios, S., 2018. Emission performance of a diesel engine fuelled with petrol diesel, green diesel, and waste cooking oil blends. J. Combust. 2018, 7–12. https://doi.org/10.3303/CET1974002.
Riza, M.A., Go, Y., Maier, R.R.J., Harun, S.W., Anas, S.B., 2020. Hygroscopic materials and characterization techniques for fiber sensing applications: a review. Sens. Mater. 32, 3755–3772. https://doi.org/10.18494/SAM.2020.2967.
Rozmysłowicz, B., Mäki-Arvela, P., Tokarev, A., Leino, A.R., Eränen, K., Murzin, D.Y., 2012. Influence of hydrogen in catalytic deoxygenation of fatty acids and their derivatives over Pd/C. Ind. Eng. Chem. Res. 51, 8922–8927. https://doi.org/10.1021/ie202421x.
Ruangudomsakul, M., Osakoo, N., Wittayakun, J., Keawkumay, C., Butburee, T., Youngjan, S., Faungnawakij, K., Poo-arporn, Y., Kidkhunthod, P., Khemthong, P., 2021. Hydrodeoxygenation of palm oil to green diesel products on mixed-phase nickel phosphides. Mol. Catal., 111422 https://doi.org/10.1016/j.mcat.2021.111422.
Sadek, R., Chalupka, K.A., Mierczynski, P., Maniukiewicz, W., Rynkowski, J., Gurgul, J., Lasoń-Rydel, M., Casale, S., Brouri, D., Dzwigaj, S., 2020. The catalytic performance of Ni-Co/Beta zeolite catalysts in Fischer-Tropsch synthesis. Catalysts 10. https://doi.org/10.3390/catal10010112.
Safa-Gamal, M., Asikin-Mijan, N., Arumugam, M., Khalit, W.N.A.W., Nur Azreena, I., Hafez, F.S., Taufiq-Yap, Y.H., 2021. Catalytic deoxygenation by H_2-free single-step conversion of free fatty acid feedstock over a Co-Ag carbon-based catalyst for green diesel production. J. Anal. Appl. Pyrolysis 160, 105334. https://doi.org/10.1016/j.jaap.2021.105334.
Serrano, D.P., Arroyo, M., Briones, L., Hernando, H., Escola, J.M., 2021. Selective decarboxylation of fatty acids catalyzed by Pd-supported hierarchical ZSM-5 zeolite. Energy Fuels 35, 17167–17181. https://doi.org/10.1021/acs.energyfuels.1c01373.
Shim, J.O., Jeong, D.W., Jang, W.J., Jeon, K.W., Kim, S.H., Jeon, B.H., Roh, H.S., Na, J. G., Oh, Y.K., Han, S.S., Ko, C.H., 2015. Optimization of unsupported CoMo catalysts for decarboxylation of oleic acid. Catal. Commun. 67, 16–20. https://doi.org/10.1016/j.catcom.2015.03.034.
Sihombing, J.L., Gea, S., Wirjosentono, B., Agusnar, H., Pulungan, A.N., Herlinawati, H., Yusuf, M., 2020. Characteristic and catalytic performance of Co and Co-Mo metal impregnated in Sarulla natural zeolite catalyst for hydrocracking of MEFA rubber seed oil into biogasoline fraction. Catalysts 10.
Silva, G.C.R., de Andrade, M.H.C., 2021. Simulation of deoxygenation of vegetable oils for diesel-like fuel production in continuous reactor. Biomass Convers. Biorefinery. https://doi.org/10.1007/s13399-021-01441-w.
Simancas, R., Chokkalingam, A., Elangovan, S.P., Liu, Z., Sano, T., Iyoki, K., Wakihara, T., Okubo, T., 2021. Recent progress in the improvement of hydrothermal stability of zeolites. Chem. Sci. 12, 7677–7695. https://doi.org/10.1039/d1sc01179k.
Somnuk, K., Soysuwan, N., Prateepchaikul, G., 2020. Optimizing three-step production of methyl ester from palm fatty acid distillate: a response surface methodology approach. Biofuels 11, 351–360. https://doi.org/10.1080/17597269.2017.1369630.
Sonthalia, A., Kumar, N., 2017. Hydroprocessed vegetable oil as a fuel for transportation sector: a review. J. Energy Inst. 1–17. https://doi.org/10.1016/j.joei.2017.10.008.
Sonthalia, A., Kumar, N., 2019. Comparison of fuel characteristics of hydrotreated waste cooking oil with its biodiesel and fossil diesel. Environ. Energy Manag.
Thongkumkoon, S., Kiatkittipong, W., Wetwatana, U., Laosiripojana, N., Daorattanachai, P., 2019. Catalytic activity of trimetallic sul fi ded Re-Ni-Mo- g-Al2O3 </sub>toward deoxygenation of palm feedstocks. Renew. Energy 140, 111–123. https://doi.org/10.1016/j.renene.2019.03.039.
Wai, K., Yusup, S., Chun, A., Loy, M., Shen, B., Skoulou, V., Taylor, M.J., 2022. Recent advances in the catalytic deoxygenation of plant oils and prototypical fatty acid models compounds: Catalysis. Process, Kinet. Mol. Catal. 523, 111469 https://doi.org/10.1016/j.mcat.2021.111469.

Wan Khalit, W.N.A., Asikin-Mijan, N., Marliza, T.S., Gamal, M.S., Shamsuddin, M.R., Saiman, M.I., Taufiq-Yap, Y.H., 2021. Catalytic deoxygenation of waste cooking oil utilizing nickel oxide catalysts over various supports to produce renewable diesel fuel. Biomass-.-. Bioenergy 154, 106248. https://doi.org/10.1016/j.biombioe.2021.106248.

Wan Khalit, W.N.A., Asikin-Mijan, N., Marliza, T.S., Safa-Gamal, M., Shamsuddin, M.R., Azreena, I.N., Saiman, M.I., Taufiq-Yap, Y.H., 2022. One-pot decarboxylation and decarbonylation reaction of waste cooking oil over activated carbon supported nickel-zinc catalyst into diesel-like fuels. J. Anal. Appl. Pyrolysis 164, 105505. https://doi.org/10.1016/j.jaap.2022.105505.

Wan Khalit, W.N.A., Tengku Azmi, T.S.M., Asikin-Mijan, N., Gamal, M.S., Saiman, M.I., Ibrahim, M.L., Taufiq-Yap, Y.H., 2020. Development of bimetallic nickel-based catalysts supported on activated carbon for green fuel production. RSC Adv. 10, 37218–37232. https://doi.org/10.1039/d0ra06302a.

Wang, H., Yan, S., Salley, S.O., Ng, K.Y.S.S., 2012. Hydrocarbon fuels production from hydrocracking of soybean oil using transition metal carbides and nitrides supported on ZSM-5. Ind. Eng. Chem. Res. 51, 10066–10073. https://doi.org/10.1021/ie3000776.

Xu, H., Lee, U., Wang, M., 2020. Life-cycle energy use and greenhouse gas emissions of palm fatty acid distillate derived renewable diesel. Renew. Sustain. Energy Rev. 134 https://doi.org/10.1016/j.rser.2020.110144.

Yan, T., Bing, W., Xu, M., Li, Y., Yang, Y., Cui, G., Yang, L., Wei, M., 2018. Acid–base sites synergistic catalysis over Mg–Zr–Al mixed metal oxide toward synthesis of diethyl carbonate. RSC Adv. 8, 4695–4702. https://doi.org/10.1039/c7ra13629c.

Yan, P., Kennedy, E., Stockenhuber, M., 2021a. Hydrodeoxygenation of guiacol over ion-exchanged ruthenium ZSM-5 and BEA zeolites. J. Catal. 396, 157–165. https://doi.org/10.1016/j.jcat.2021.02.013.

Yan, P., Li, M.M.-J., Kennedy, E., Adesina, A., Zhao, G., Setiawan, A., Stockenhuber, M., 2019. The role of acid and metal sites in hydrodeoxygenation of guaiacol over Ni/Beta catalyst. ⟨https://doi.org/10.1039/C4CY00072B⟩.

Yan, P., Mensah, J., Drewery, M., Kennedy, E., Maschmeyer, T., Stockenhuber, M., 2021b. Role of metal support during ru-catalysed hydrodeoxygenation of biocrude oil. Appl. Catal. B Environ. 281, 119470 https://doi.org/10.1016/j.apcatb.2020.119470.

Yang, X., Lv, B., Lu, T., Su, Y., Zhou, L., 2020. Promotion effect of Mg on a post-synthesized Sn-Beta zeolite for the conversion of glucose to methyl lactate. Catal. Sci. Technol. 10, 700–709. https://doi.org/10.1039/c9cy02376c.

Yu, S., Yan, J., Lin, W., Long, J., Liu, S.Bin, 2021. Effects of Lanthanum incorporation on stability, acidity and catalytic performance of Y zeolites. Catal. Lett. 151, 698–712. https://doi.org/10.1007/s10562-020-03357-y.

Zanuttini, M.S., Peralta, M.A., Querini, C.A., 2015. Deoxygenation of m-Cresol: deactivation and regeneration of Pt/γ-Al_2O_3 catalysts. Ind. Eng. Chem. Res. 54, 4929–4939. https://doi.org/10.1021/acs.iecr.5b00305.

Zhang, L., Gao, J., Hu, J., Li, W., Wang, J., 2009. Lanthanum oxides-improved catalytic performance of ZSM-5 in toluene alkylation with methanol. Catal. Lett. 130, 355–361. https://doi.org/10.1007/s10562-009-9965-3.

Zhang, Z., Wang, Q., Chen, H., Zhang, X., 2017. Hydroconversion of waste cooking oil into green biofuel over hierarchical USY-Supported NiMo catalyst: a comparative study of desilication and dealumination. Catalysts 7. https://doi.org/10.3390/catal7100281.

Zhao, X., Wei, L., Cheng, S., Huang, Y., Yu, Y., Julson, J., 2015. Catalytic cracking of camelina oil for hydrocarbon biofuel over ZSM-5-Zn catalyst. Fuel Process. Technol. 139, 117–126. https://doi.org/10.1016/j.fuproc.2015.07.033.

Zuo, H., Zhang, Q., Liu, Q., Wang, T., Ma, L., 2013. One-step hydrodeoxygenation of palm oil to isomerized hydrocarbon fuels over Ni supported on nano-sized SAPO-11 catalysts. Appl. Catal. A Gen. 468, 68–74. https://doi.org/10.1016/j.apcata.2013.08.009.